EFFECTS OF CORIOLIS FORCE ON LIQUID FUEL WICK FLAMES IN ARTIFICIAL PARTIAL GRAVITY IN A CENTRIFUGE

by

ARLAND ZATANIA LOJO

Submitted in partial fulfillment of the requirements for the degree of

Master of Science

Department of Mechanical and Aerospace Engineering

CASE WESTERN RESERVE UNIVERSITY

January, 2023

CASE WESTERN RESERVE

SCHOOL OF GRADUATE STUDIES

We hereby approve the thesis/dissertation of

Arland Zatania Lojo

candidate for the degree of Master of Science *.

Committee Chair

Ya-Ting Liao, PhD

Committee Member

Paul Barnhart, PhD

Committee Member

Bryan Schmidt, PhD

Committee Member

Paul Ferkul, PhD

Committee Member

Michael Johnston, PhD

Committee Member

Ankit Sharma, PhD

Date of Defense

December 2, 2022

*We also certify that written approval has been

obtained for any proprietary material contained therein.

To my parents,
Emil and Esmeralda,
My sister,
Ona,
And all my friends,
Without whom none of my success would be possible

Table of Contents

List of Tables

List of Figures

Nomenclature

ΔH_c^0	heat of combustion (J/kg)
$\frac{\epsilon}{k}$	turbulent mixing rate (s^{-1})
$\vec{\Omega}$	angular velocity (s^{-1})
β	angle between velocity and the x axis (deg)
θ	angle between $\vec{F}_T$ and the x axis (deg)
$\nu'_{i,r}$	stoichiometric coefficient for reactant, *i,* in reaction, *r* (-)
$\nu''_{i,r}$	stoichiometric coefficient for product, *i,* in reaction, *r* (-)
ρ	density (kg/m^3)
$\bar{\bar{\tau}}_r$	viscous stress tensor (N/m^2)
A	empirical constant equal to 4.0 in Equation 2.7 (-)
B	empirical constant equal to 0.5 in Equation 2.7 (-)
E_r	relative internal energy (J)
$\vec{F}_B$	buoyancy force per unit volume (N/m^3)
$\vec{F}_T$	sum of Coriolis and buoyancy force (N/m^3)
H_r	relative total enthalpy (rothalpy) (J)
J_i	mass diffusion flux of species, *i* (g/m^2s)
$M_{\omega,i}$	molecular weight of species, *i* (g/mol)
N	number of chemical species in system (-)
$\dot{Q}$	heat release rate (W)
$R_{i,r}$	net rate of production species, *i,* due to reaction, *r* (kg/s)

S_h	heat of chemical reaction (J/mol)
S_i	rate of creation by addition from the dispersed phase (-)
T	temperature (K)
X	x position (m)
Y_{o2}	mass fraction of oxygen (-)
Y_i	mass fraction of species, I (-)
Y_P	mass fraction of any product species, P (-)
$Y_{\mathcal{R}}$	mass fraction of a particular reactant, $\mathcal{R}$ (-)
Z	z position (m)
a_c	Coriolis acceleration (m/s^2)
g	gravity (m/s^2)
g_c	centrifugal acceleration (m/s^2)
g_e	earth's gravity (m/s^2)
$\dot{m}$	mass flow rate (kg/s)
p	pressure (Pa)
$\vec{r}$	position vector (m)
t	time (s)
$\vec{v}_r$	relative velocity vector (m/s)

Acknowledgements

I want to thank Dr. Ya-Ting Liao for first hiring me as a member of her lab in January 2020 and then becoming my advisor as she encouraged me to do research and pursue a master's degree. In addition, I am extremely grateful for all the support that Dr. Ankit Sharma has given me throughout the completion of this project. I also thank both Dr. Liao and Dr. Sharma for their encouragement in applying to the ICES and ASGSR conferences.

I also want to show gratitude to Dr. Paul Ferkul, and Dr. Michael Johnston for sharing experimental data and providing valuable inputs.

Previous efforts by former undergraduate students Jonah Sachs-Wetstone and Andrew Green (CWRU) are also acknowledged.

Continuous conversations with Dr. Chengyao Li about his work are acknowledged. Who is also working on modeling a convective heat transfer simulation under artificial gravity in a rotating enclosure.

This work is supported by NASA Glenn Research Center under Award #NNX16AL61A and Award #80NSSC22M011.

The numerical study made use of the High-Performance Computing Resource in the Core Facility for Advanced Research Computing at Case Western Reserve University.

Effects of Coriolis Force on Liquid Fuel Wick Flames

in Artificial Partial Gravity in a Centrifuge

Abstract

by

ARLAND ZATANIA LOJO

Numerical simulations are performed to support a combustion experiment campaign in partial gravity in a centrifuge designed for use in conjunction with the NASA Glenn Research Center's Zero Gravity Research Facility (a 5.2 second drop tower). The centrifuge is a circular dome chamber of volume ~ 0.3 m^3 with 81.3 cm diameter. The artificial gravitational field is controlled by the rotation rate of the chamber. This is complicated by gravitational gradients as a function of radius and by Coriolis force as a function of flow velocity. The model is constructed with Ansys FLUENT utilizing a rotating non-inertial reference frame and simulates the entire chamber volume containing a heptane candle with a wick length of 10 mm × 3.18 mm diameter located at 32 cm from the centrifuge center. Simulation results locally near the candle are compared to a series of experiment images where the flame tip bends in the Coriolis force direction. The study investigates the recirculation effects and the relation between the buoyancy and the Coriolis force in how they affect the flame. The model simulates the experiments well and suggestions are made to avoid recirculation effects in future centrifuge experiments.

1 Introduction

1.1 Motivation and Background

The safety of spacecraft and astronauts in space is of utmost importance for any space research and exploration mission. In addition to various biological and physiological challenges, fire hazard is a serious concern due to limited evacuation and fire suppression options. Furthermore, fire behavior is remarkably different in microgravity compared to normal gravity due to the absence of buoyancy. There are scenarios where, for other conditions being the same, combustion occurs in reduced gravity but not in normal gravity [1]. It has also been observed that steady flame spread can be achieved in microgravity in concurrent flows, whereas on Earth, flame spread is usually regarded as an acceleratory process for typical fuel bed sizes [2], [3]. These fundamental differences in flame behavior have prompted many experimental studies to develop a better understanding of fire dynamics in reduced and microgravity conditions using drop towers [4], [5], parabolic flights [6], [7], space shuttles [8], and facilities aboard the International Space Station [9].

For future missions such as NASA's Artemis program, there are plans to send humans to the Moon for Lunar exploration and research. This program will include the establishment of a new space station in Lunar orbit (Gateway) and eventually the creation of a habitable Lunar base for further exploration (e.g., to Mars). These new missions bring a unique set of challenges due to the gravity level on the Moon, which is $1/6^{th}$ of Earth's gravity (g_e). It is well known that buoyancy plays a significant role in fire growth processes in normal gravity [10]. However, reduced

buoyancy conditions in partial gravity can create unique fire hazards compared to normal gravity. The expected weaker buoyancy flow in partial gravity can lead to smaller convective heat loss and a longer residence time of reactants in the flame stabilization zone. As a result, a material may be combustible over a wider range of oxygen concentrations and pressures in partial gravity than in normal gravity. Therefore, studying how a fire would behave in these partial gravity conditions becomes very important for the safe continuation of space exploration in such environments.

1.2 Previous Related Works

There have been only a few studies [1], [6], [7], [11], [12] on partial gravity flame behavior due to limited opportunities in performing experiments. Feier et al.[6] performed upward and downward flame spread and extinction experiments over a thin solid in an artificial partial gravity environment created in an airplane flying parabolic trajectories. A linearly increasing relationship with gravity was observed for flame spread rates and pyrolysis lengths with proportionality constants dependent on the pressure and sample width. They also developed a three-dimensional numerical model and obtained good agreement with the experiment. Kleinhenz et al. [7] experimentally verified this dependence of upward flame spread on pressure and gravity over thin solids.

Another way to generate artificial gravity is by using a centrifuge. This technique has been used in some of the previous studies [13] to generate hypergravity by rotating the centrifuge in Earth's normal gravity and allowing the

sample fixture to swing in order to be aligned with the net acceleration vector. In order to generate artificial *partial* gravity levels, the centrifuge needs to be rotated in a microgravity facility (e.g., drop tower, orbiting space vehicle, parabolic flight). However, one of the complications for rotating reference frames using a centrifuge facility is the Coriolis force. When hot combusting gas "rises" toward the axis of rotation, it experiences a Coriolis force orthogonal to the velocity vector, tilting the flame and rising gases away from the radial line. Furthermore, burning experiments using a centrifuge will need to be contained in a closed combustion chamber. If the chamber is not large enough, additional challenges, including induced flow due to recirculation in the limited space of the chamber, and oxygen depletion (especially for thick samples), are present. The time duration of these experiments is also limited by the hosting microgravity platform (e.g., ~5 s for drop tower, 20-30s for parabolic aircraft flights, and 1-2 minutes for sounding rockets) and operations can be costly.

1.3 Research Gaps

Due to these difficulties in setting up an artificial partial gravity environment, there have been only a handful of experimental studies [6], [7] on flame dynamics in partial gravity. This leads to a need for more research to be done in this area to understand fully the fire behaviors in partial gravities.

These challenges can be overcome using Computational Fluid Dynamics (CFD) techniques to understand experimental results and design future partial gravity tests. Some previous studies have developed numerical models for studying

partial gravity flame spread [14], [15]. However, to the author's best knowledge, there are no numerical studies that specifically investigated the effect of flame behavior in the partial gravity environment created using a centrifuge.

1.4 Objectives

The objective of the present study is to study the behavior of flames in partial gravity as well as the effects that Coriolis force and recirculation have on the shape and development of the flames. In this work, a numerical model is developed and validated with previous NASA experiments. The effects of Coriolis force and flow recirculation are discussed. The long-term goal is to provide guidance for the design of future centrifuge tests and provide information on how the results from centrifuge burning tests could be interpreted.

2 Numerical Model

The numerical model is constructed based on previous microgravity experiments by Ferkul [16]. In this study, numerical simulations are carried out through the commercial CFD software ANSYS FLUENT 20.1. It is based on the Finite Volume Method (FVM) to discretize and solve the partial differential equations of continuity, energy, momentum, species transport, and turbulence modeling [15]. The geometrical CAD model is created in SolidWorks and the mesh is created in ANSYS Mechanical [17]. Experimental data for the numerical model validation has been taken from previous work [16] performed at the NASA Glenn Research Center and will be discussed in Chapter 3.

2.1 Model Configuration

The original experiments consisted of a simulated candle (i.e., a porous metal wick saturated with liquid fuel) placed horizontally over a table (XZ plane) inside a rotating dome shaped chamber as shown in Figure 2-1. Liquid fuel is drawn through the wick from the small liquid-fuel reservoir via capillarity. The chamber is dropped in a drop tower, and different artificial gravity levels are generated depending upon the angular velocity of the rotating table. The chamber is capable of producing a minimum rotation of 0.01 RPS (revolutions per second) and a maximum rotation of 1.1 RPS. Two cameras were fixed inside the chamber to record orthogonal views of the flame growth process. For carrying out numerical simulations, a 3D CAD model of the chamber has been constructed, as shown in Figure 2-2. Dimensions of the model and wick are shown in Figure 2-3 through Figure 2-5. The wick points

radially inward on the rotating table and the location of its tip is at a distance of 32 cm from the axis of rotation (+Y) (Figure 2-5).

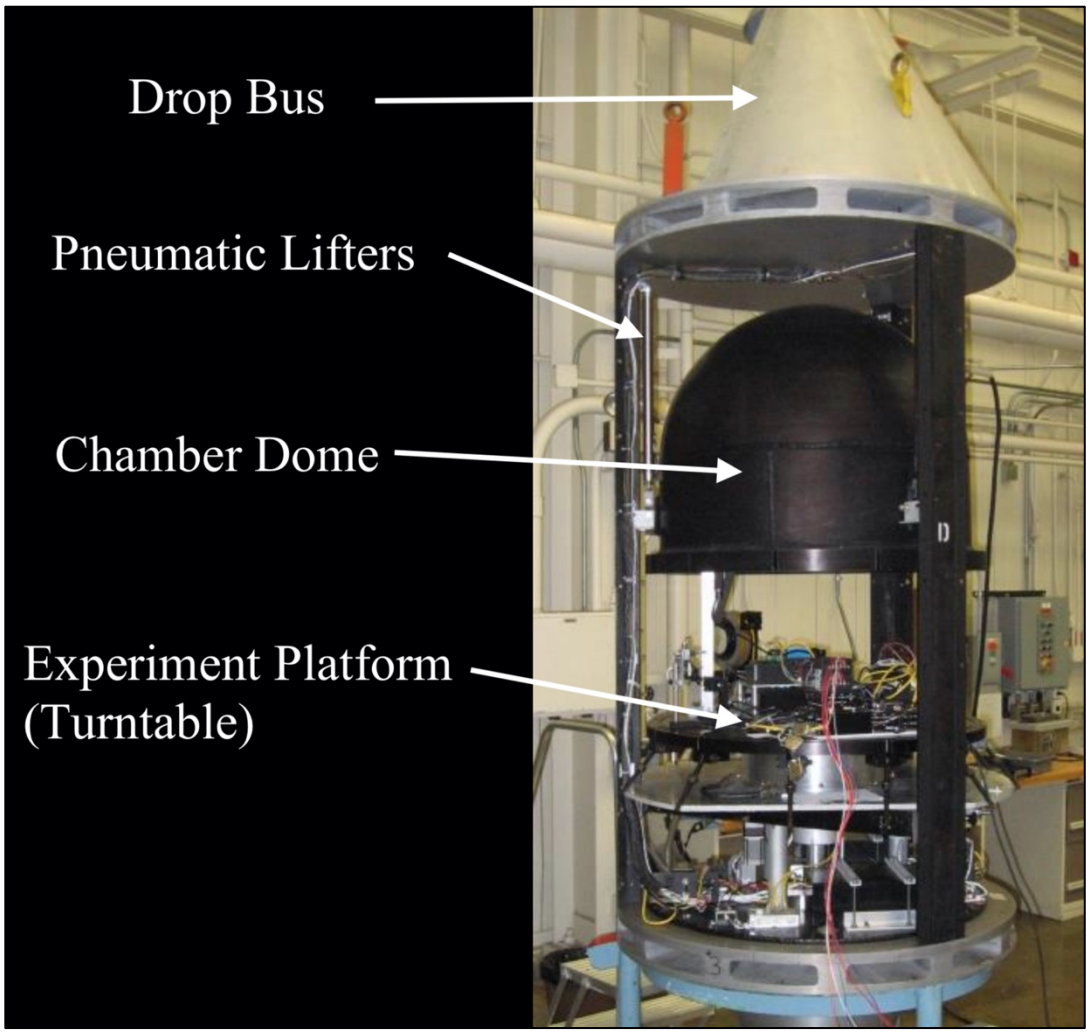

Figure 2-1. 3D experimental set up. Picture reproduced from [16]

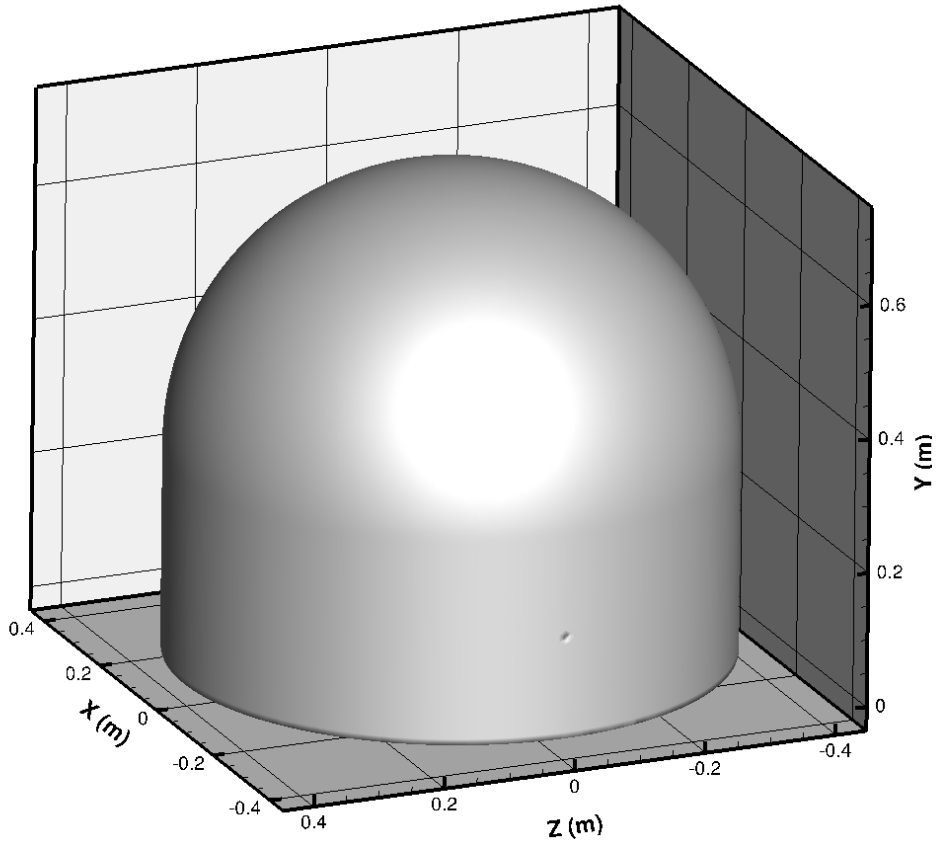

Figure 2-2. 3D CAD model for the numerical model

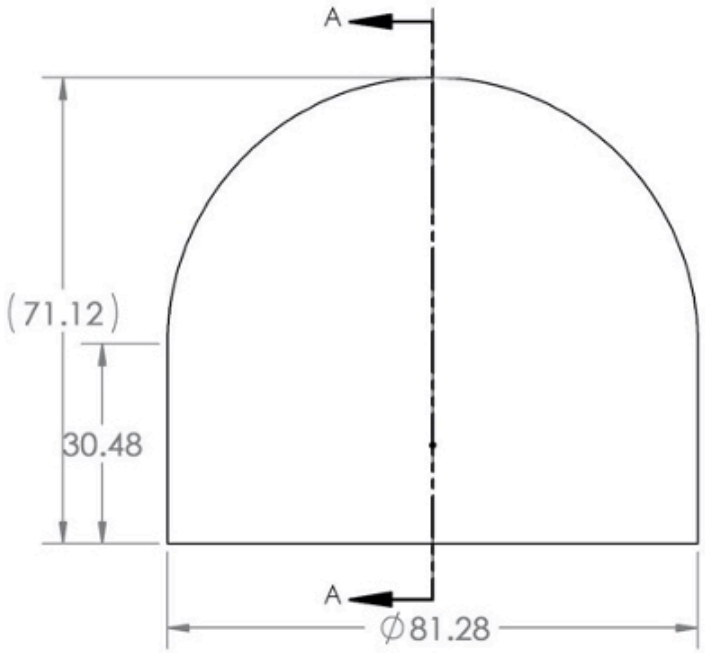

Figure 2-3. 2D sketch of the simulation domain (all dimensions in cm)

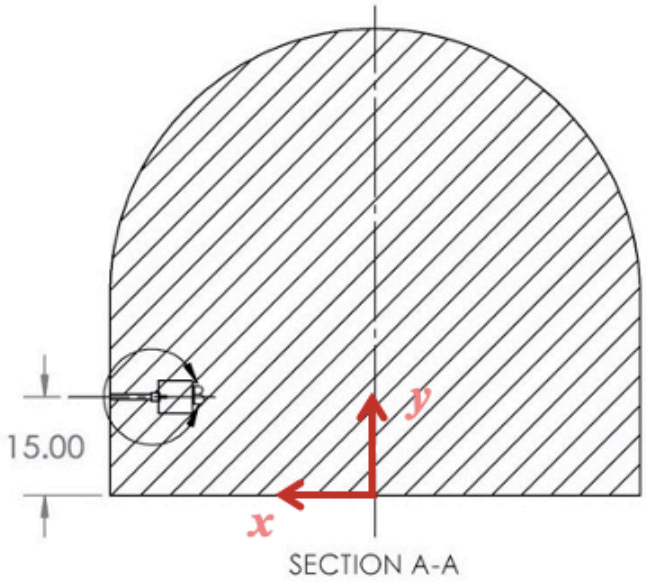

Figure 2-4. Cross section of the XY plane of the simulation domain geometry at z = 0 (all dimensions in cm)

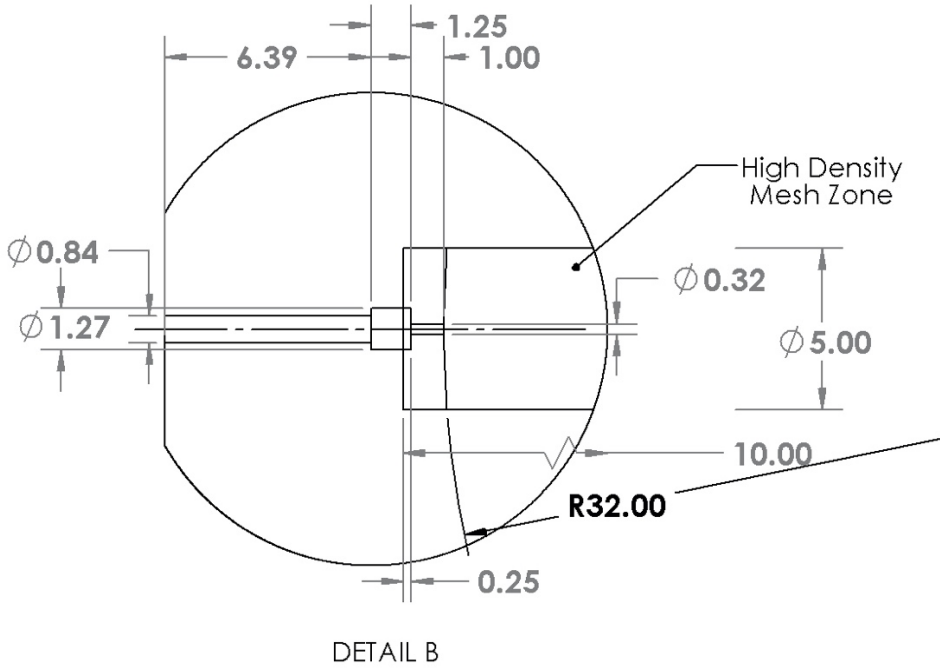

Figure 2-5. Detailed view of the inlet (circled in Figure 2-4). All dimensions are in cm.

2.2 Numerical Formulation

This section presents a summary of the important equations and boundary conditions that the numerical model implements. Since the simulation has a rotating reference frame, the continuity, momentum, and energy equations take cylindrical form.

For the gas-phase combustion, the reaction is assumed to be single step overall stoichiometric combustion: $C_7H_{16} + 11O_2 \rightarrow 8H_2O + 7CO_2$. This assumption is valid for the current simulation as gaseous heptane fuel coming out of the wick burns fast and the overall rate of reaction is controlled by turbulent mixing. Thus, the eddy dissipation model is selected against the finite-rate model. In addition, inlet diffusion and a diffusion energy source were also enabled which respectively include the diffusive flux of species at the inlet and the effect of enthalpy transport due to species diffusion. Inlet diffusion is used so that the net transport of energy at the inlet has convective and diffusive components. Otherwise, convection would only be used. The diffusion energy source is activated so that the inlet temperature is specified in the setup rather than the net transport of energy.

Turbulence is modeled using the Reynolds-averaged Navier–Stokes (RANS) equations with a k-omega SST model.

It is assumed that gas phase radiation has minimum impact on the modeling results for the small flames simulated in this work (especially in micro- and reduced gravities). Furthermore, in the current model, fuel mass flux on the wick surface is fixed at a pre-defined value (to be discussed further in Sec. 2.2.2) and does not

depend on the flame heat feedback. For these reasons, gas phase radiation was not modeled to save computation time.

2.2.1 Governing Equations

Conservation of mass [18]:

$$\frac{\partial \rho}{\partial t} + \nabla \cdot \rho \vec{v}_r = 0 \tag{2.1}$$

Conservation of momentum [18]:

$$\frac{\partial}{\partial t}(\rho \vec{v}_r) + \nabla \cdot (\rho \vec{v}_r \vec{v}_r) + \rho\left(2\vec{\Omega} \times \vec{v}_r + \vec{\Omega} \times \vec{\Omega} \times \vec{r}\right) = -\nabla p + \nabla \cdot \bar{\bar{\tau}}_r \tag{2.2}$$

In this equation the Coriolis acceleration appears as:

$$2\vec{\Omega} \times \vec{v}_r \tag{2.3}$$

And the centripetal acceleration as:

$$\left(\vec{\Omega} \times \vec{\Omega} \times \vec{r}\right) \tag{2.4}$$

Conservation of energy [18]:

$$\frac{\partial}{\partial t}(\rho E_r) + \nabla \cdot (\rho \vec{v}_r H_r) = \nabla \cdot (k \nabla T + \bar{\bar{\tau}}_r \cdot \vec{v}_r) + S_h \tag{2.5}$$

Conservation equation for chemical species [18]:

$$\frac{\partial}{\partial t}(\rho Y_i) + \nabla \cdot (\rho \vec{v} Y_i) = -\nabla \cdot \vec{J_i} + R_i + S_i \tag{2.6}$$

The following equations are used to get the net rate of production species *i* due to reaction *r*. The value is taken to be the smaller of the two equations below:

$$R_{i,r} = \nu'_{i,r} M_{\omega,i} A \rho \frac{\epsilon}{k} \min_{\mathcal{R}} \left(\frac{Y_{\mathcal{R}}}{\nu'_{\mathcal{R},r} M_{\omega,\mathcal{R}}} \right) \tag{2.7a}$$

$$R_{i,r} = \nu'_{i,r} M_{\omega,i} A B \rho \frac{\epsilon}{k} \frac{\sum_P Y_P}{\sum_j^N \nu''_{j,r} M_{\omega,j}} \tag{2.7b}$$

2.2.2 Initial and Boundary Conditions

Boundary Conditions:

In order to approximate the NASA Glenn experiments [16] as close as possible, the boundary conditions are carefully chosen. A typical candle flame has a total power output of 75 to 100W [19]. Based on this, mass flow rate of liquid through the wick was selected to produce a 100W flame. A constant mass flux of 2.08×10^{-6} kg/s is then assumed on the wick surface in the model in order to match a 100 W candle flame:

$$\dot{m} = \frac{\dot{Q}}{\Delta H_c^0} \tag{2.8}$$

The inlet temperature for the heptane was chosen to be 500 K since that would guarantee it is above its boiling point (371.6 K) [20] at the chamber experiment pressure (1 atm). Note that in the experiments, the evaporation rate of the wick depends on the heat feedback from the flame. While the assumption of constant mass flux used in the numerical model does not perfectly mimic the behavior of the wick in the experiment, it was selected for the sake of simplicity in this initial study.

To generate the artificial gravity, the computational domain is rotated around the vertical (i.e., *y*-) axis. The rotational speeds were selected to match experimental values to generate 0 g_e, 0.003 g_e, 0.012 g_e, 0.075 g_e, 0.2 g_e, 0.3 g_e, 0.59 g_e, and 1 g_e at the location 30 cm (r) from the axis of rotation. While the wick is at 32 cm from the axis of rotation, the gravity is evaluated at 30 cm since that is

approximately the center of the flame. Table 2-1uses Equation 2.9 to determine the corresponding angular velocity for each acceleration tested.

$$\Omega = \sqrt{\frac{g_e}{r}} \tag{2.9}$$

Table 2-1. Acceleration vs. Angular Velocity

Acceleration (g_e)	0	0.003	0.012	0.075	0.2	0.3	0.59	1
Angular Velocity (rad/s)	0	0.313	0.626	1.566	2.557	3.132	4.392	5.717

A constant time step (0.01 s) was used (Section 2.4), and each simulation was run for a total 500 timesteps in order to obtain a full 5 s of data. 5 s is chosen based on the duration of the experiments (~5.18 s) in the drop tower setup [16]. All walls were defined as no-slip (with respect to the rotating frame) and adiabatic conditions.

Table 2-2. Boundary conditions and time step information

Inlet Mass Flux	2.08×10^{-6} kg/s
Inlet Temperature	500 K
Angular Velocity	Table 2-1. Acceleration vs. Angular Velocity
Walls	No-slip Adiabatic
Time step size	0.01 s
Timesteps	500
Iterations per Timestep	20

Initial Conditions:

The initial conditions are chosen to mimic the experimental setup. As discussed in Equation 2.7a and 2.7b, the eddy-dissipation model requires a small amount of reaction products in the domain to start the initial reaction or the reaction rate will always be zero. The model is therefore initialized with conditions matching that of air with 23.13% mass fraction O_2 and 0.05% mass fraction of H_2O

and CO_2. The remainder is all set to be N_2. These initial contents of the chamber are set to have a temperature of 300 K which matches ambient air temperature.

Note that in the actual experiments, the chamber is initially spun up before it is dropped so that all of the air inside is in solid body rotation. This has been considered in the simulations and all masses are setup to start in rotation.

The following table is a summary of the initial conditions for the model.

Table 2-3. Initial Conditions

Chamber Temperature		300 K
Mass Fraction	H_2O	0.05%
	CO_2	0.05%
	O_2	23.13%
	N_2	76.77%
Initial Relative Velocity		0 m/s

2.3 Mesh Study

As shown in Figure 2-6, non-uniform meshing is used to optimize computational time and resources with finer mesh near the wick where the flame is expected to grow. The resulting overall domain consists of 8.14 million cells with the largest cell of volume 8.89×10^{-7} m^3 and the smallest being 8.21×10^{-12} m^3. A finer mesh is also allocated near the walls to accurately resolve the thermal and viscous boundary layers.

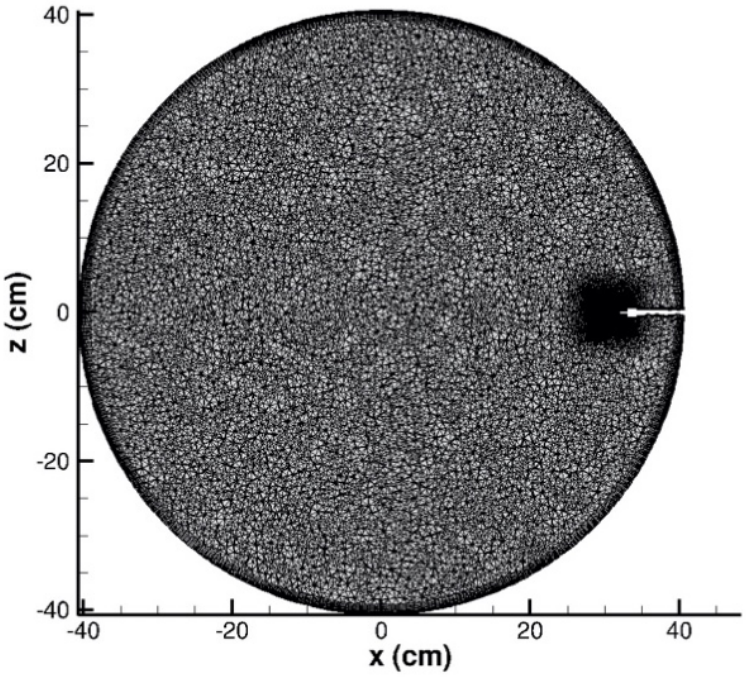

Figure 2-6. XZ Plane view of Mesh at y = 0.15 cm

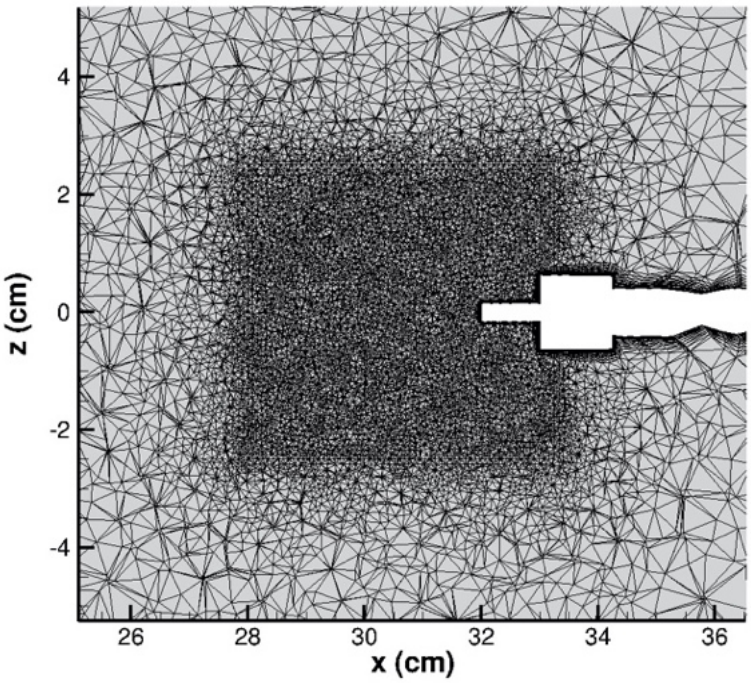

Figure 2-7. Detailed view of inlet on XZ Plane view of Mesh at y = 0.15 cm

To ensure that the mesh resolution is appropriate a study was done comparing a more refined mesh (shown in Figure 2-8) and a less refined mesh (shown Figure 2-9 in). These have a total of 9.32 and 1.35 million cells respectively. All three meshes were set up for an artificial 1g rotation flame. The temperature contours at 1 s are shown in Figure 2-10. It is observed that the contours have the same length and curvature for the mid- and high-density mesh demonstrating that the mid-density for this numerical study is appropriate. In addition, Table 2-4 has some quantitative values from both flames. It can be observed that the high- and mid-density flames have a much smaller difference for a considerable time saving than the low-density flame.

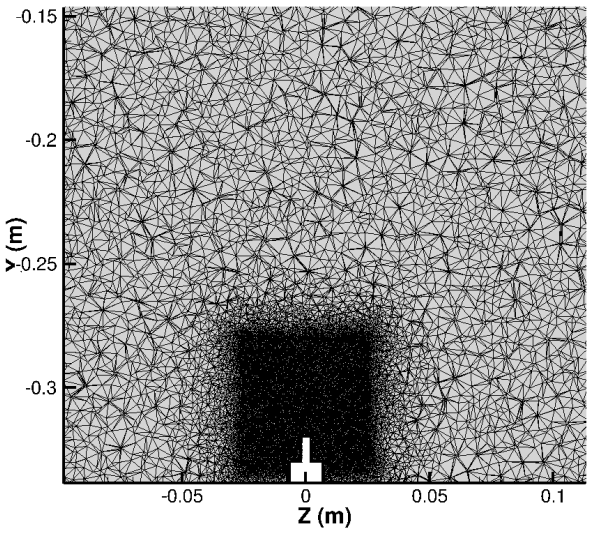

Figure 2-8. High resolution mesh: 9.32 million cells

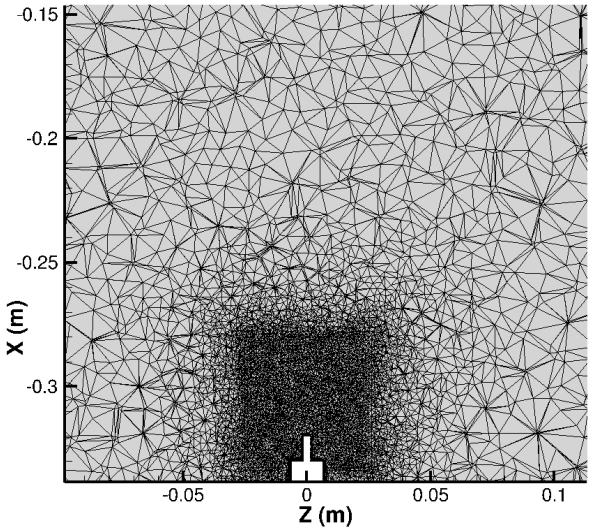

Figure 2-9. Low resolution mesh: 1.35 million cells

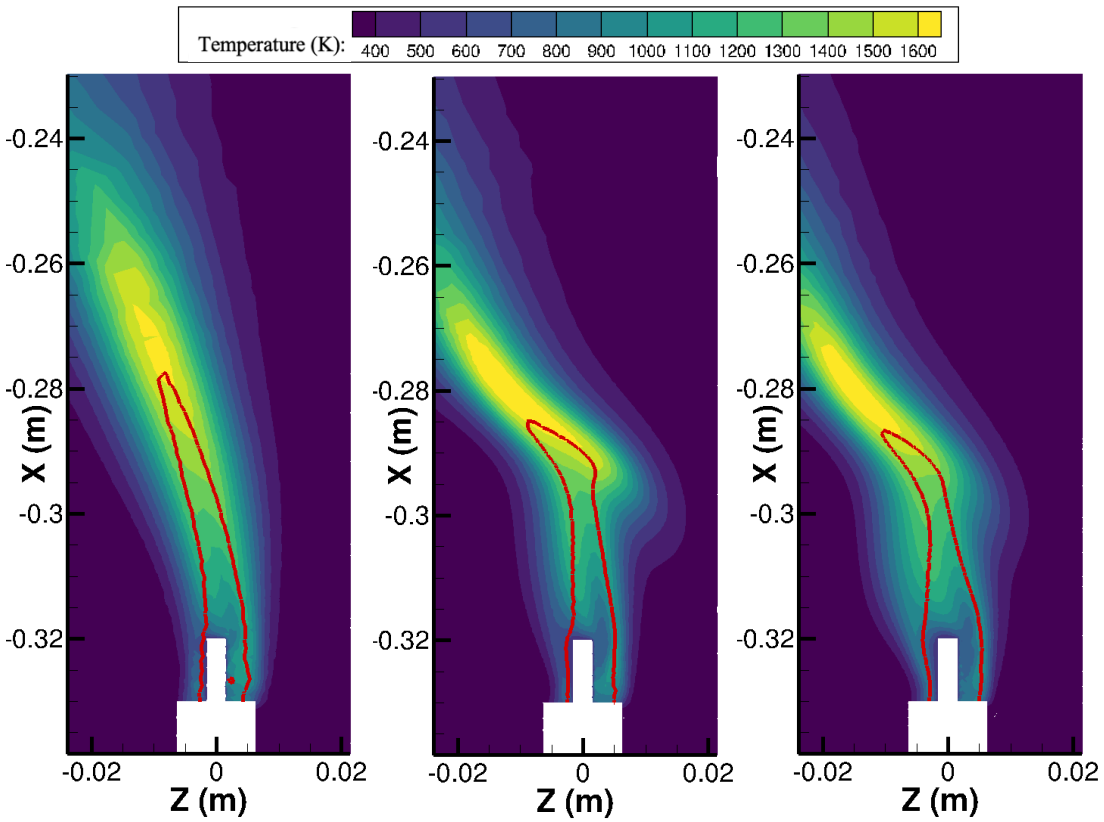

Figure 2-10. X_{02} = 0.05 contours for the low-, mid-, and high-density mesh flame (left to right) for rotational $1g_e$ at 1 s.

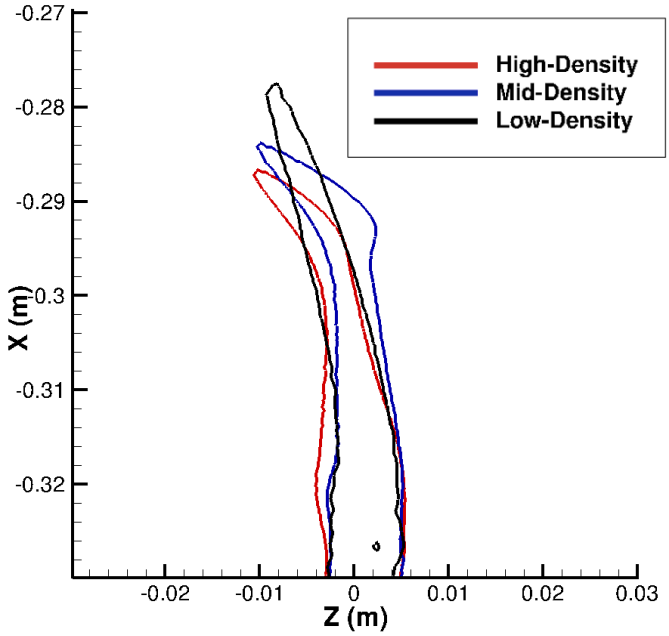

Figure 2-11. Overlapped X_{02} = 0.05 contours for the low-, mid-, and high-density mesh flame for rotational $1g_e$ at 1 s.

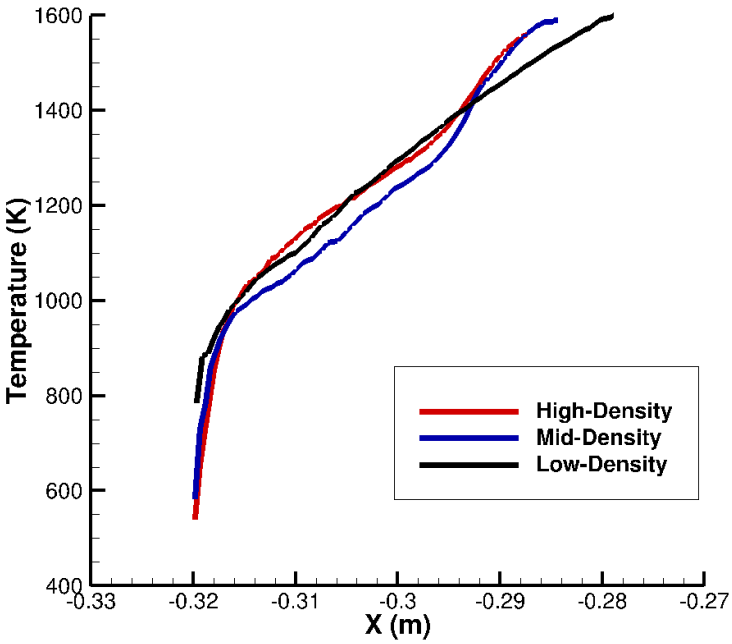

Figure 2-12. Flame temperature centerline for the low-, mid-, and high-density mesh flame for rotational $1g_e$ at 1 s.

Table 2-4. Comparison of low-, mid-, and high-density mesh flames

Criteria	**High-Density Mesh**	**Mid-Density Mesh**	**Low-Density Mesh**
Cell Ammount	9.32E6	8.14E6	1.35E6
Max. Temp	1701 K	1795 K	1669 K
	100%	~105%	~98%
Max. Coriolis acceleration	12,4 m/s^2	12,6 m/s^2	15,3 m/s^2
	100%	~101%	~123%
Computational Time Percentage Difference	100%	~87%	~15%

2.4 Time Independence Study

A timestep of 0.01 s is selected for the simulations. This timestep is selected because it gives the minimum resolution that we want to obtain from the simulation. However, to make sure that this is good enough, the same 1 g_e case used in the mesh study is run with a smaller time step of 0.005 s. Figure 2-13 shows how they both compare at t = 1 s. Figure 2-14 further compares both cases overlapping their contours at t = 1s and t = 1.4 s. These times are shown since they are the top and bottom of a flame pulsation. Also, Table 2-5 has some quantitative values from both flames. It can be observed that not much difference exists between both simulation results when compared to the saved computational time.

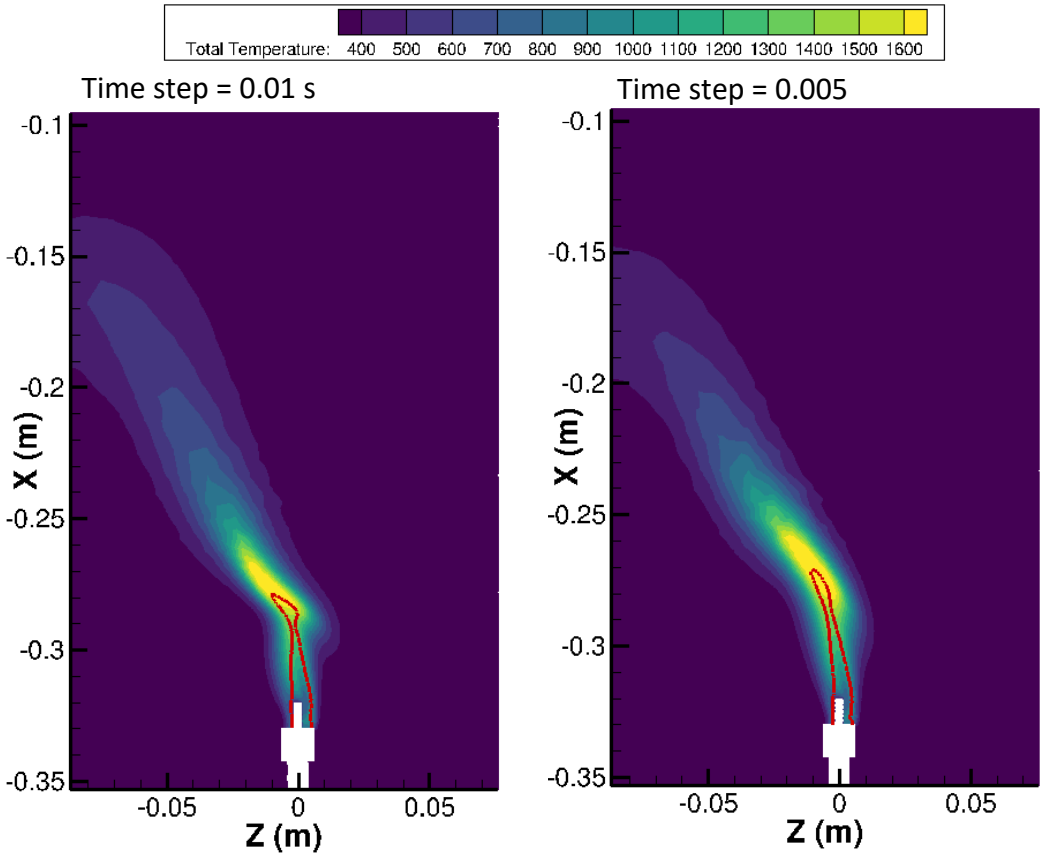

Figure 2-13. X_{02} = 0.05 contours for the 0.01 s and the 0.005 s timestep cases for rotational $1g_e$ at 1 s.

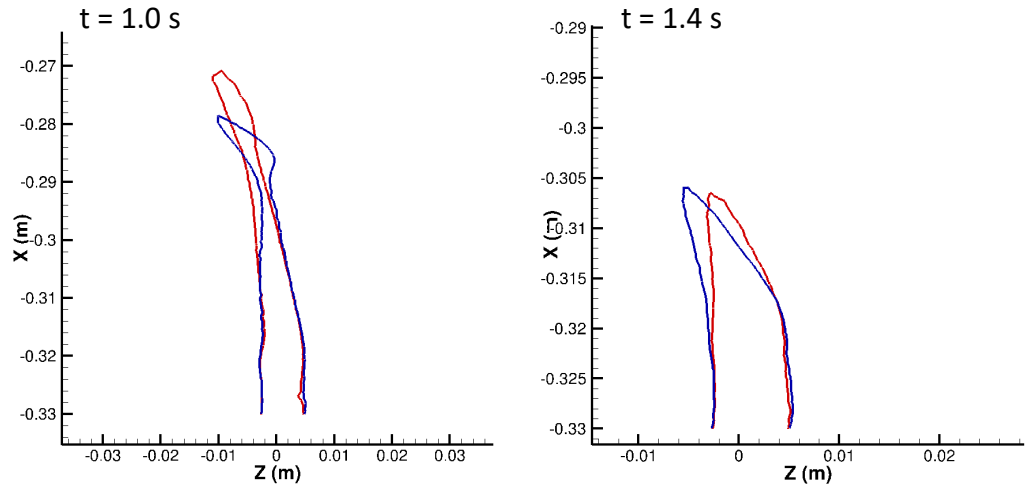

Figure 2-14. Overlapped X_{02} = 0.05 contours for the 0.01 s and the 0.005 s timestep cases for rotational $1g_e$ at 1 s, and 1.4 s.

Table 2-5. Comparison of 0.01 s and 0.005 s time-step flames

Criteria	**0.01 s**	**0.005 s**
Max. Temp	1795 K	1800 K
	~100%	100%
Max. Coriolis acceleration	12,6 m/s2	13,7 m/s2
	~91%	100%
Computational Time	~50%	100%

3 Validation against Partial Gravity Experiments

3.1 Transient Flame Growth Process

Figure 3-1 shows a side-by-side comparison of the flame growth process in the experiment (left panes) and in the present simulation (right panes) for artificial gravity at 0.3 g_e. Images are 0.3 s apart. Numerical results display the temperature contour with a 5% (mass fraction) oxygen isoline (black line). Note that in literatures, different variables (e.g., gas temperature, gas-phase reaction rate, concentration of oxygen, concentration of product gas) have been used to represent flame shape. Here a consistent criterion of 5% oxygen concentration was used in all simulated cases.

It can be seen that the numerical simulation predicts a flame shape similar to that in the experiments. Results indicate a close resemblance of the experimental flame shape through the entire flame development process. After ignition, the flame grows “upwards” towards the center of rotation and turns towards the left due to the effect of Coriolis force both in experiments and simulations. This is discussed in detail in Sec. 4.2.

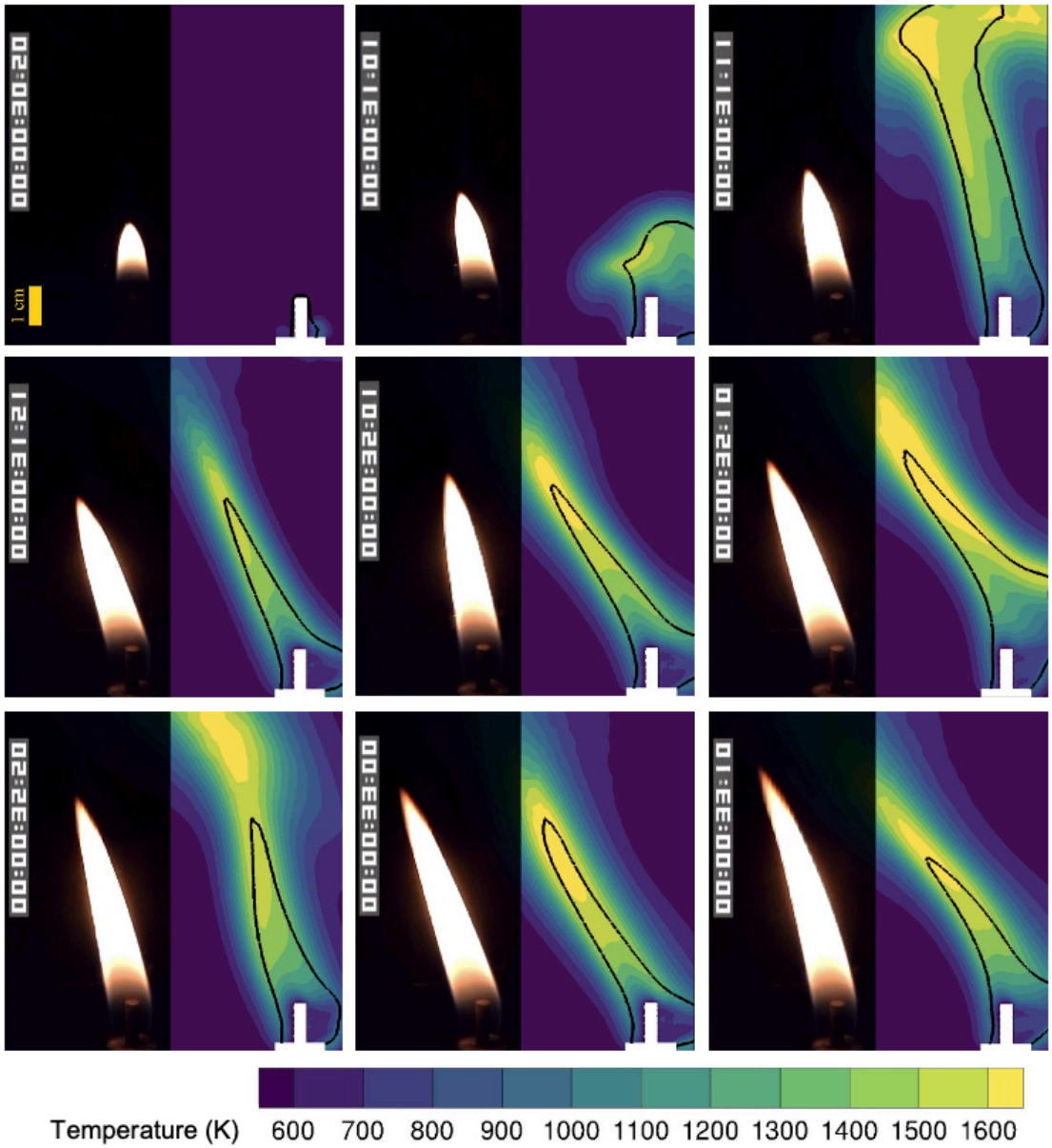

Figure 3-1. Comparison of the flame growth between experiment (left) and numerical simulation (right) in the first 3 s at an equal interval of 0.3 s (left to right, top to bottom). The black lines in the numerical simulation (right) are the isolines of oxygen mass fraction of 5%. Artificial gravity level: 0.3 g_e.

3.2 Flame shapes at different gravity levels

Figure 3-2 compares the flame images in both experiment and simulation results at different artificial gravities. A good agreement is observed between experimental and simulation results. Note that for cases with artificial gravity

greater than 0.075 g_e, flame pulsing was observed both in the experiments and in the numerical results. Images in Figure 3-2 capture the instances when flames reach maximum length in all cases. By qualitative comparison, the maximum flame length follows a similar increasing trend with an increase in gravity level. It is also observed that the dependence of the flame tilt angle on artificial gravity is similar in the experimental and numerical results. When the artificial gravity increases from 0 to 0.012 g_e, the flame transitions from a spherical to a slightly elongated elliptical shape with no obvious tilt. As the artificial gravity increases to above 0.075 g_e, the flame tilts to the left. The tilt angles remain similar in all tested artificial gravity levels. This is because the Coriolis effect and artificial gravity are both proportional to the rotational angular velocity and is discussed in detailed in Sec. 4.2.

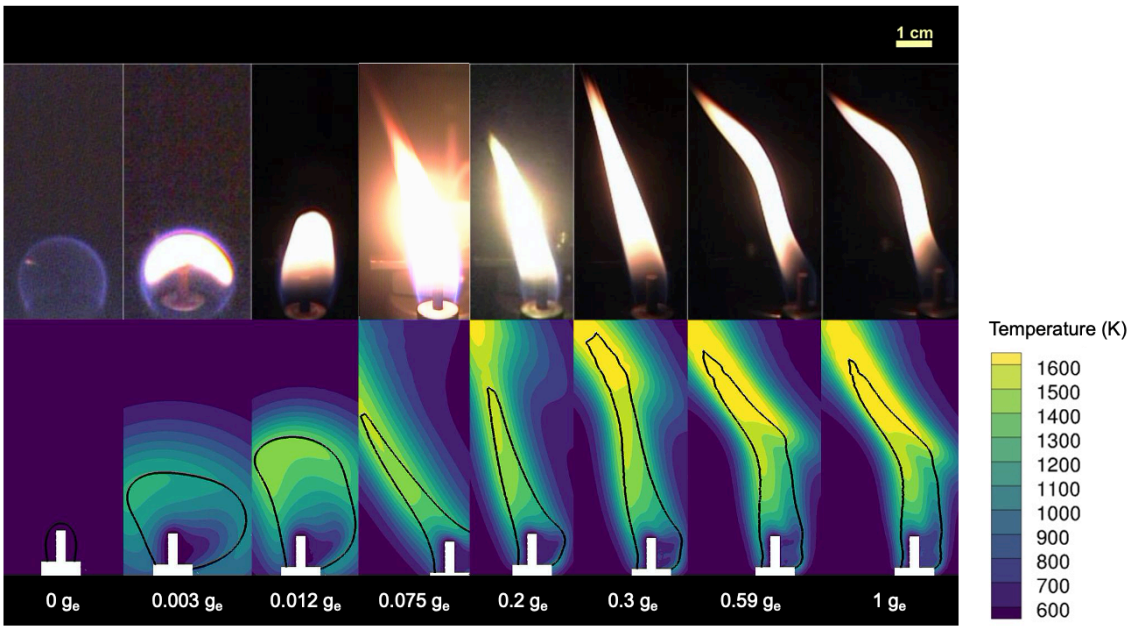

Figure 3-2. Comparison of the flame shape in different artificial gravity levels (top: experiment; bottom: simulation). The black lines in the numerical simulation (bottom) are the isolines of oxygen mole fraction of 5%. These images are chosen at best matching time steps at the maximum flame length.

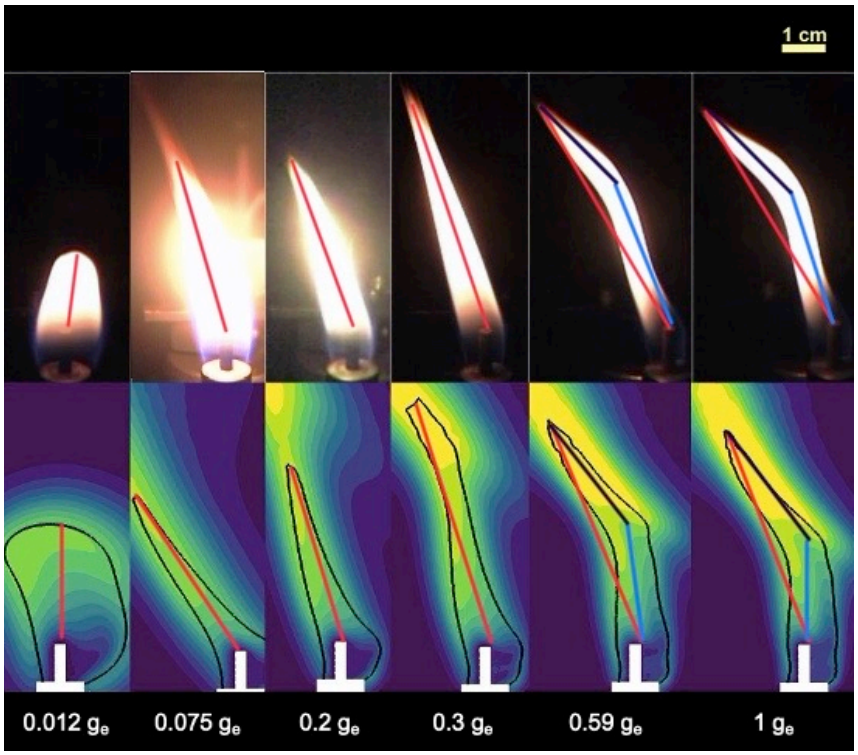

Figure 3-3. Root to tip lines (in red), root to bend lines (in blue), and bend to tip lines (in purple)

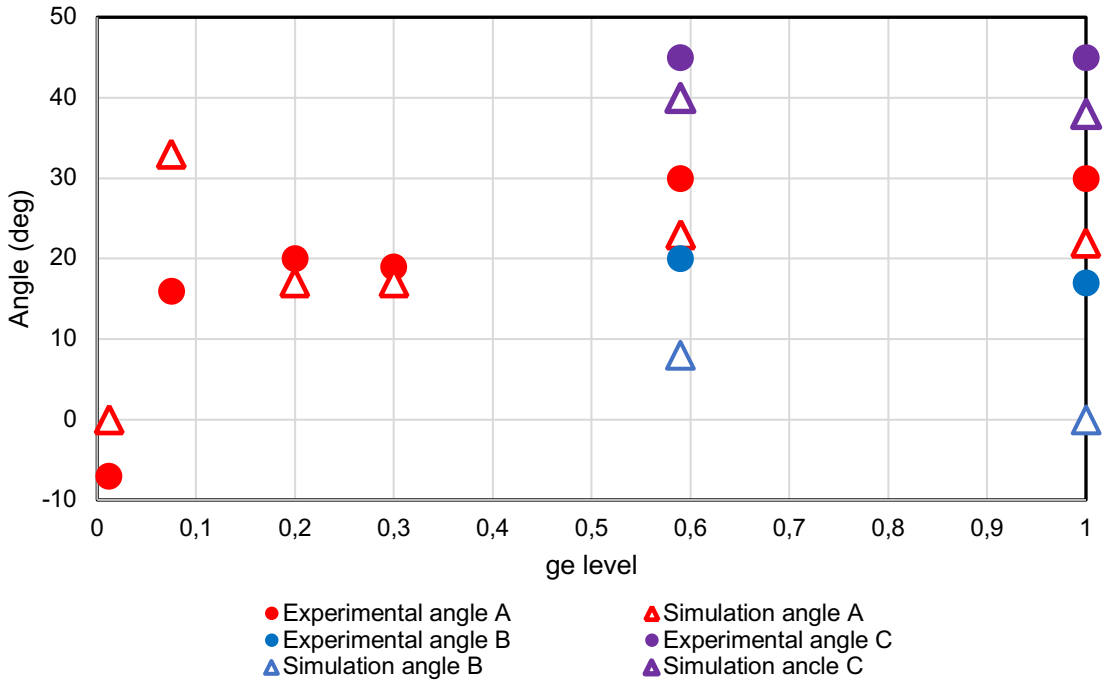

Figure 3-4. Experimental and simulation flame angle at maximum length for different given g_e levels

4 Results

4.1 Artificial Gravity and Coriolis Effect

Since the centrifuge is rotating in the microgravity facility inside the drop tower, it does not experience normal Earth's gravity, but everything within the rotating chamber experiences an outward centrifugal acceleration g_c (i.e., artificial gravity acting outwards along the radius of the centrifuge):

$$g_c = -\Omega \times (\Omega \times r) = -\Omega^2 r \tag{4.1}$$

Here ω is the angular velocity (rad/s) of the rotating centrifuge, and r is the position vector (r = 0 is the axis of rotation). The artificial gravity is proportional to radius of rotation as shown in Equation 4.1. Figure 4-1 shows the vectors of artificial (centrifugal) gravity corresponding to the case of 1 g_e. In this case, the flame (defined as Y_{o2} = 0.05) is ~ 6.4 cm long and the artificial gravity varies from ~ 8.17 to 10.46 m/s^2 (corresponding to 0.83 g_e – 1.07 g_e) in the flame region with 1ge at 30 cm from the axis of rotation (Figure 4-2).

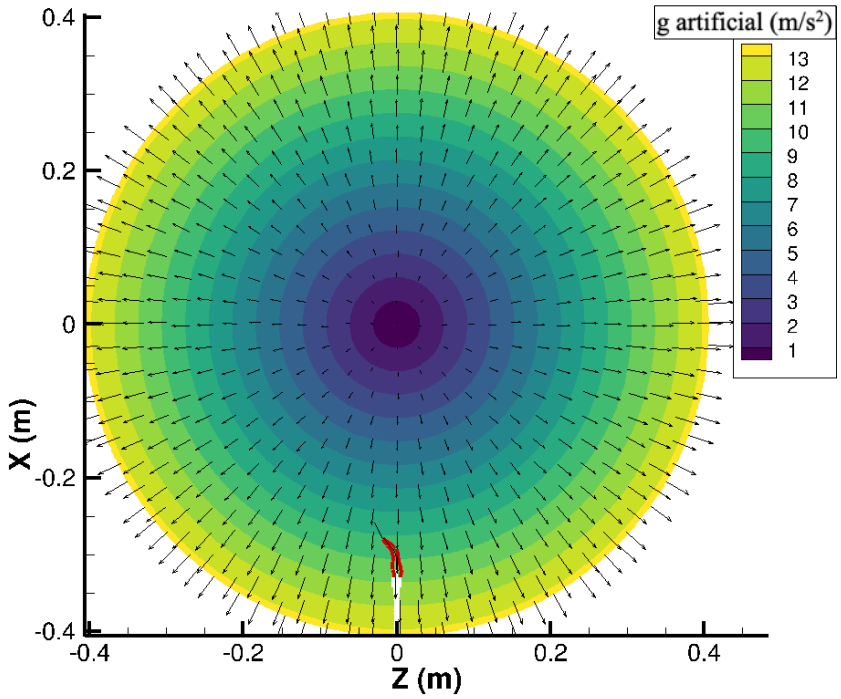

Figure 4-1. Distribution of the artificial gravity on the rotating table in the case of 1 g_e. The red line shown is the isoline of oxygen mole fraction at 5%

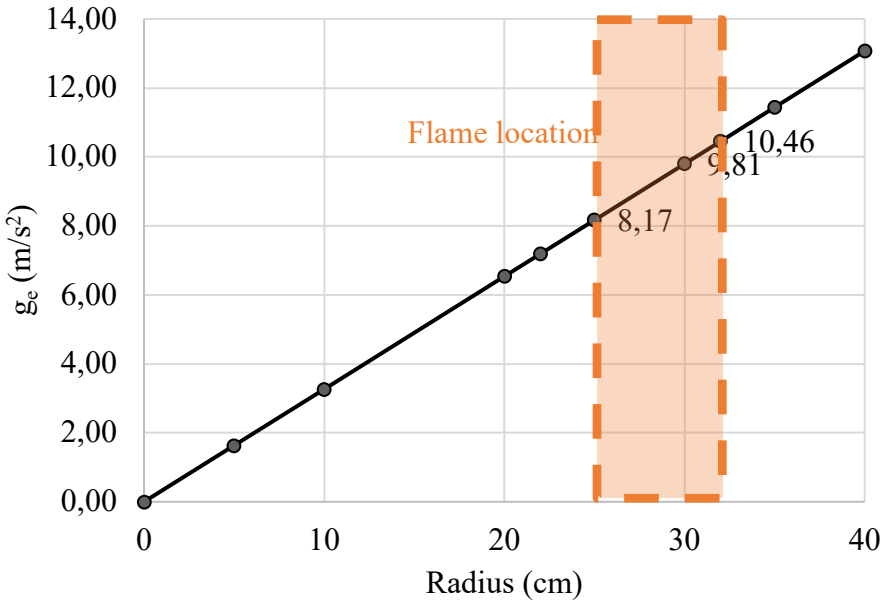

Figure 4-2. Artificial gravity depending on the radius location in the case of 1 g_e. The orange region encompasses the location of the flame

After combustion is initiated near the wick, hot combustion products rise to the rotating center due to the artificial gravity buoyancy force (in the positive x-direction). In the meantime, the Coriolis force tilts the flame in the tangential direction as seen in Figure 4-4. The Coriolis acceleration ($\vec{a}_c$) is:

$$\vec{a}_c = -2\vec{\Omega} \times \vec{v}_r \tag{4.2}$$

Here, $\vec{v}_r$ is the velocity vector. All velocities, streamlines, and accelerations in this paper are presented with respect to the rotating reference frame. The streamlines and contours of magnitude are shown on . The magnitude (contour colors) and direction (black arrows) of Coriolis acceleration are shown in Figure 4-4. The effect of Coriolis force can be seen as the flame is being pushed in the negative *z*-direction. Note that the Coriolis direction acts perpendicularly to the velocity as it is expected from Equation 4.2.

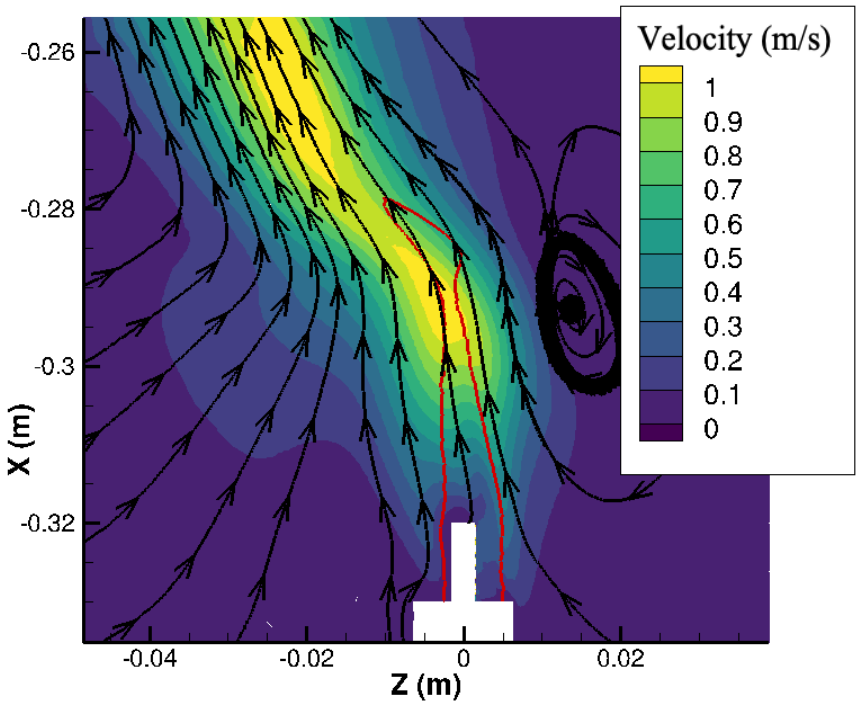

Figure 4-3. Velocity for artificial gravity 1 g_e. Streamlines show direction of velocity (1 s)

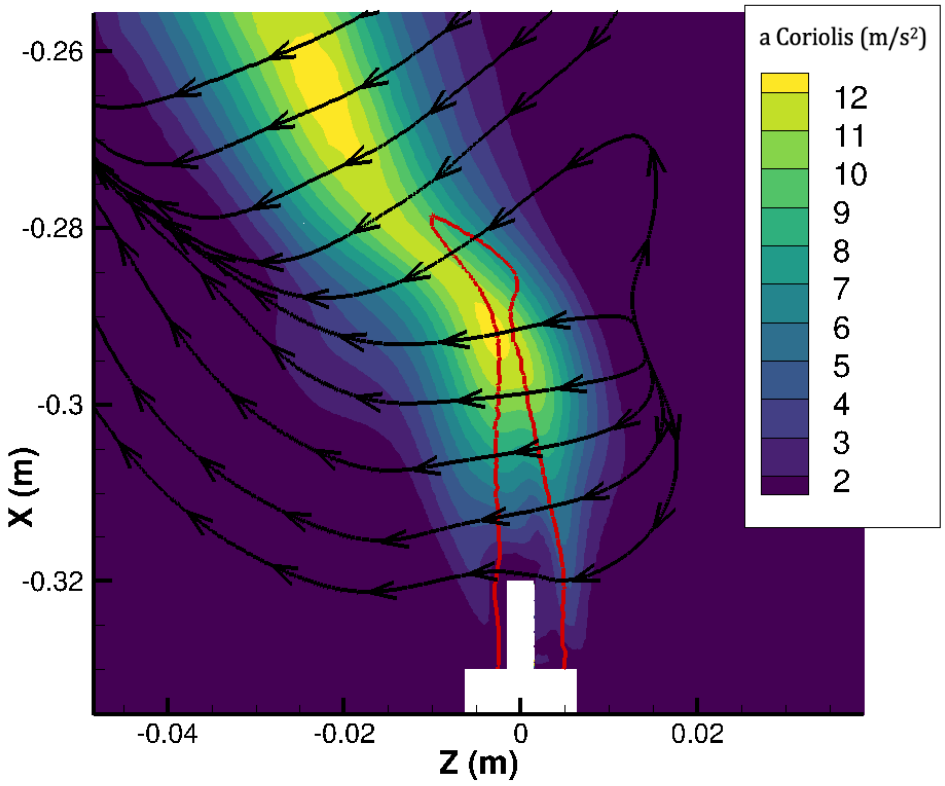

Figure 4-4. Coriolis acceleration for artificial gravity 1 g_e. Arrows show direction of Coriolis acceleration (1 s)

In all simulated cases (except the 0 g_e rotating and the 1 g_e non-rotating case), the flame experiences tangential flows caused by the Coriolis force.

Also, note that the tangential flow (caused by the effects of Coriolis force) leads to Coriolis acceleration in the radial direction (see Equation 4.2 and Figure 4-6) since the Coriolis force always acts orthogonally to the flow direction. Figure 4-5 and Figure 4-6 show the magnitudes (color contours) of the radial and tangential components of the Coriolis acceleration respectively. If the radial component of $\vec{a}_c$ is comparable to the centrifugal acceleration, it contributes to the artificial gravity and should not be overlooked. Further analysis and comparisons of a_c in different gravity levels will be pursued in the next section.

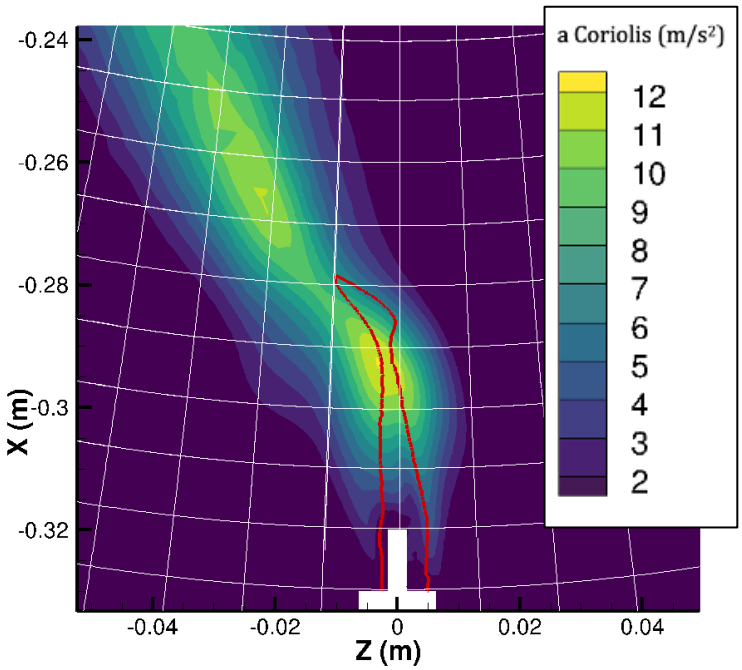

Figure 4-5. Tangential Coriolis acceleration for 1 g_e simulation, red line is oxygen at 5%, white lines are radial direction

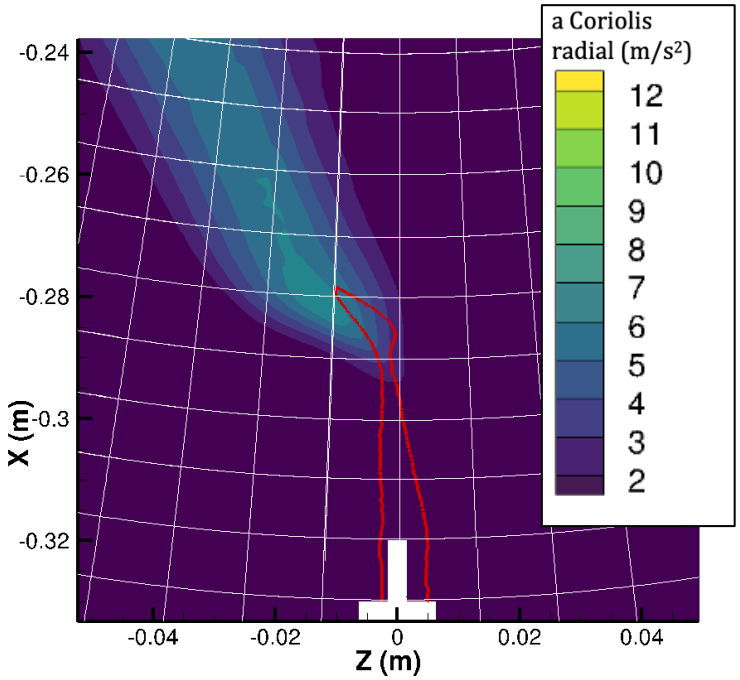

Figure 4-6. Radial Coriolis acceleration for 1 g_e simulation, red line is oxygen at 5%, white lines are radial direction

Figure 4-5 and Figure 4-6 show how the Coriolis acceleration first increases in the tangential direction and then as the flame inclines, the Coriolis acceleration starts increasing in the radial direction and decreasing in the tangential direction until it seems to tilt back and increase in the tangential direction.

Figure 4-7 compares the magnitude and direction of Coriolis acceleration for different artificial g levels. Coriolis acceleration was observed to be decreasing with decreasing g levels. Figure 4-8, Figure 4-9, and Figure 4-10 further indicate that the maximum Coriolis acceleration decreases linearly with decreasing artificial gravity. In all cases, the maximum Coriolis acceleration at some points in the domain is larger than the artificial gravity. This will be discussed in Section 4.2 where a relation between gas temperature, flow velocity and buoyancy force will be made in order to understand how and why the flame tilts.

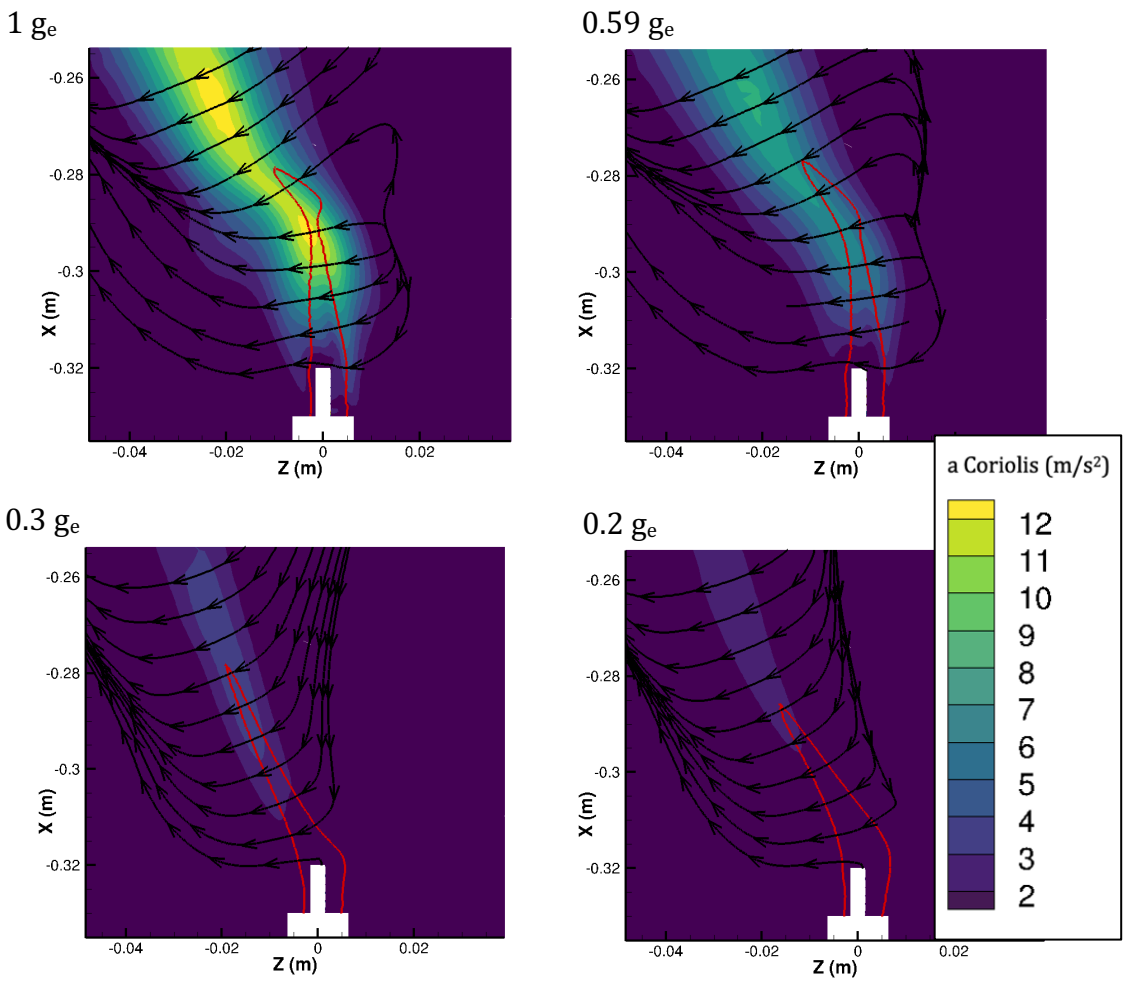

Figure 4-7. Contours of Coriolis acceleration (m/s²) at different artificial gravity levels at the flames' longest length.

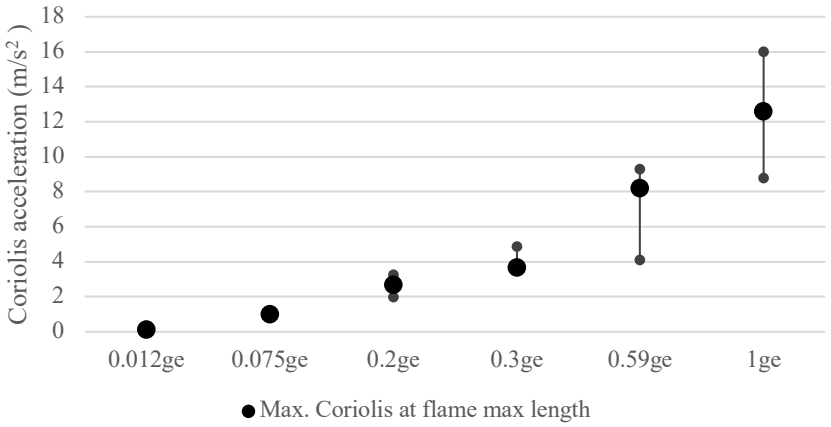

Figure 4-8. Max. Coriolis acceleration vs. partial gravity. Vertical lines represent range of max. Coriolis acceleration throughout the 5 seconds of simulation once the flame has developed

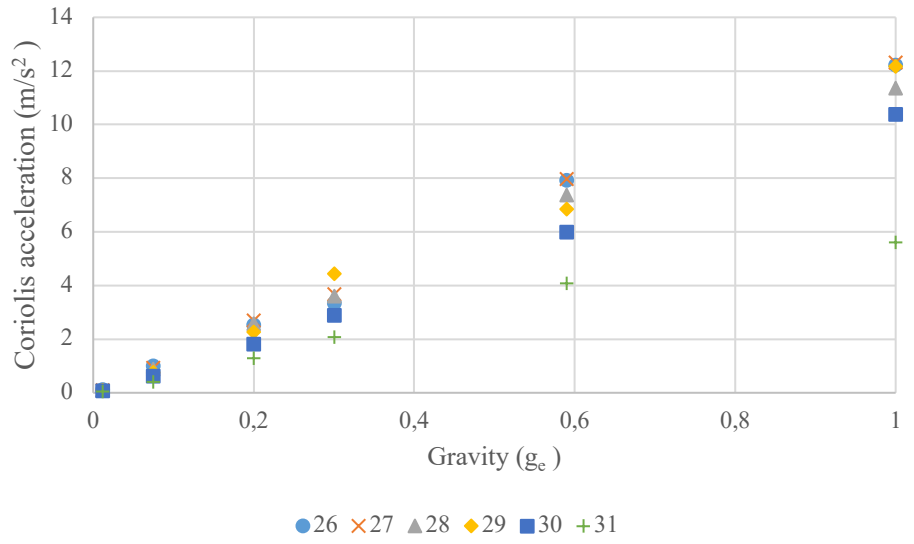

Figure 4-9. Coriolis acceleration vs. partial gravity at different radii of the maximum length flame

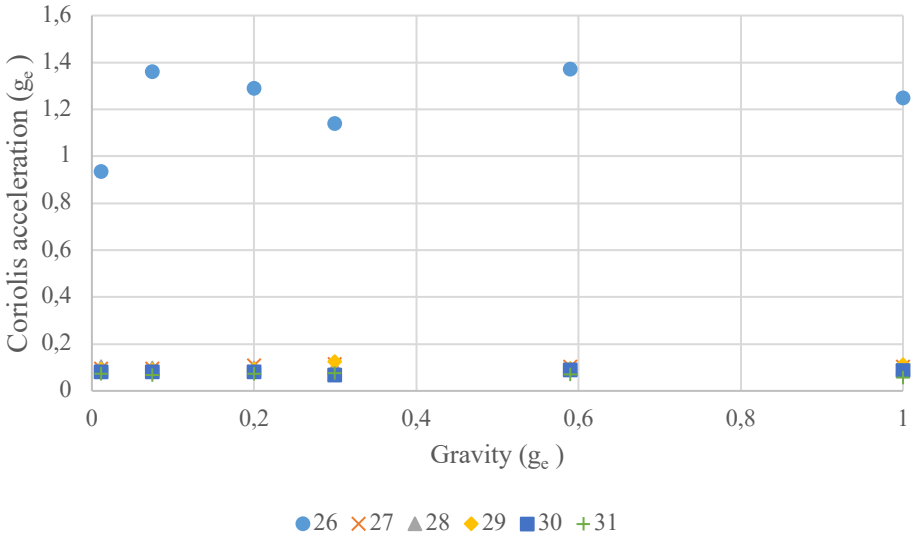

Figure 4-10. Non-dimensional Coriolis acceleration (by earth gravity 9.81 m/s²) vs. partial gravity at different radii of the maximum length flame

4.2 Flame Tilt Angles

To better understand the tilt and bend of the flame, results were analyzed to understand all the forces involved and how they behave throughout the flame zone. Buoyancy force per unit volume is evaluated using the following equation:

$$F_B = g_c \cdot (\rho - \rho_0) \tag{4.3}$$

Where ρ_0 is the density of the ambient air at 300K.

From the equation, it can be seen clearly how buoyancy depends on the density which in turn depends on the temperature. Figure 4-11 shows the relation between the buoyancy force and temperature. Since the buoyancy force depends on temperature, one can notice that the maximum vectors for the force are located over the maximum temperature zones.

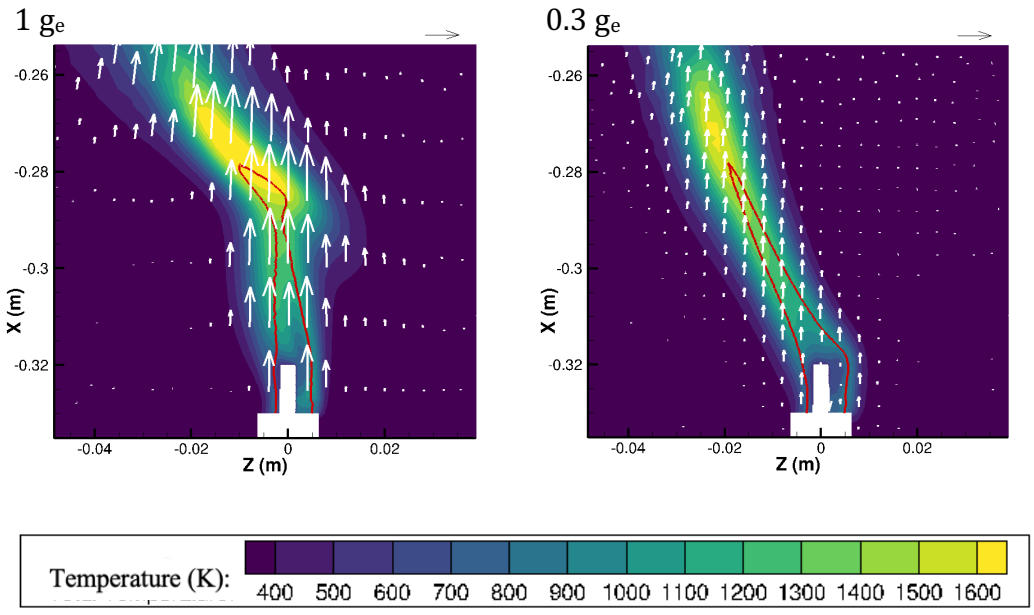

Figure 4-11. Total temperature contours and vectors of buoyancy force for 1 and 0.3 g_e. Unit vector (shown on the upper right in each plot) is 5N/m^3 .

Coriolis was discussed in the previous section. However, Figure 4-12 further expands our understanding of how this force behaves throughout the flame. In the figure it is clearly visible how the Coriolis force peaks at the place where its relative velocity is at its maximum in accordance with Equation 4.2.

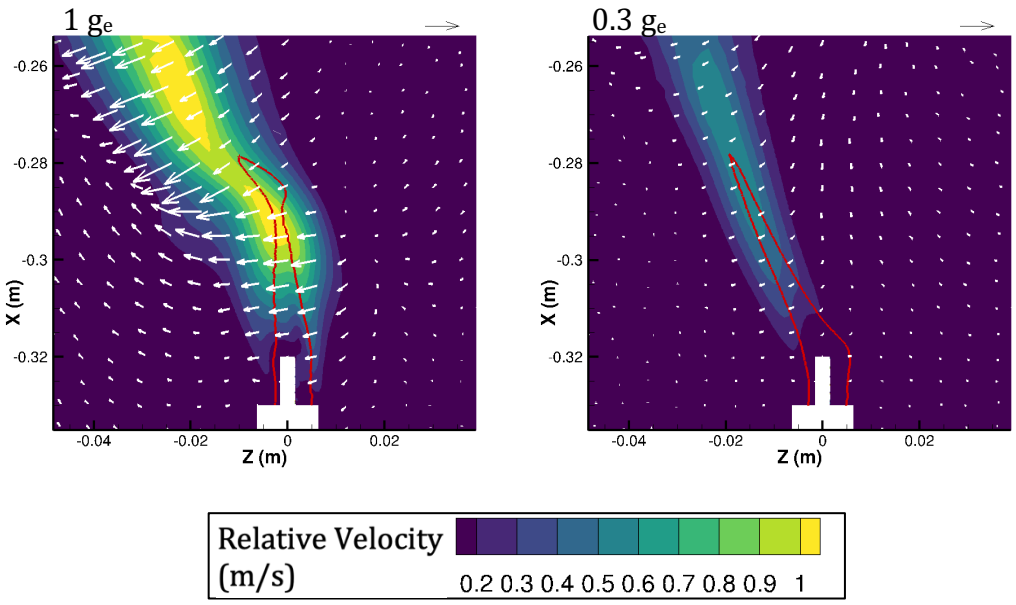

Figure 4-12. Relative velocity contours and vectors of Coriolis force for 1 and 0.3 g_e

Figure 4-13 shows the combination of both forces. We can see how the combined force vectors follow the angle of the flame from base to tip..

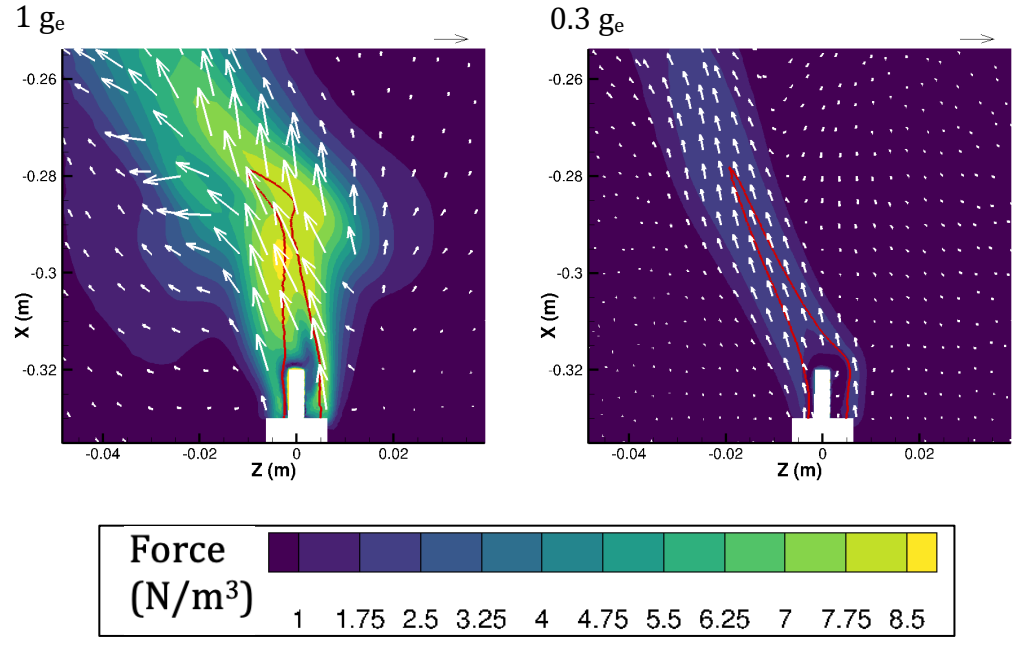

Figure 4-13. Total force contours and vectors for 1 and 0.3 g_e

The flame tilt angle is the angle between the buoyancy force and the combined buoyancy and Coriolis forces, this angle is given by:

$$\theta = \tan^{-1}\left(\frac{-F_{T,z}}{F_{T,x}}\right) \tag{4.4}$$

The buoyancy force here is selected because it always acts on the radial direction so the equation always gives the angle between the radial direction and the total force.

To see the angle between the flame and the radial direction, a similar equation is used substituting the total force vector with the relative velocity vector:

$$\beta = \tan^{-1}\left(\frac{-v_{r,z}}{v_{r,x}}\right) \tag{4.5}$$

Figure 4-14 shows the these two angles vs. the coordinate *X*. It can be seen how these equations relate to the flame bending. The flame starts at a shallow angle β with the total forces at an angle θ. There is a moment where β starts to increase as the flame bends at which point θ decreases. θ increases slightly before the bend because as seen in Figure 4-5, the tangential Coriolis force increases at that point. Then, right after the bend, θ decreases since as shown in Figure 4-5 and Figure 4-6, the Coriolis force in the tangential direction decreases while it increases in the radial direction opposite from the center. For the 0.2 g_e case, since there is no bend, θ and β have the same value throughout the flame.

Figure 4-15 shows the entire behavior of the flame bending and why it happens. The flame begins at a small angle β (~8°) in which the air begins to heat up. As it heats up we can see the buoyancy force increase which leads to an increase in the relative velocity in the *x*-direction. This increase in velocity increases the Coriolis force onto the flame which then visually bends the flame. After the bend, the velocity in the *x*-direction gets smaller and so does the Coriolis force. During the

time of the bend, the buoyancy force is still increasing so β gets smaller again causing a visible rectification of the flame.

Unlike the 1 g_e flame, the 0.3 g_e flame does not have the bend. Figure 4-16 shows how the forces, temperature and relative velocity relate.

Note that the sharp change in θ for 0.3 g_e is caused by the thermal plume not being fully developed yet after x = -0.22 m. Figure 4-17, Figure 4-18, and Figure 4-19 combine data from Figure 4-15 and Figure 4-16 so they can be compared easily. It is observed in Figure 4-17 how the angle θ is similar. However, the angle β is different since the 0.3g_e flame does not experience the same bending that the 1g_e flame experiences. A further look into Figure 4-18 shows how during the bend that the 1g_e flame experiences the velocity in the x-direction is lowered and so is the Coriolis force, while the 0.3g_e flame doesn't experience this since it doesn't bend. Finally, Figure 4-19 shows how while both flames have similar temperatures, they have very different magnitudes for the buoyancy force due to the differences in artificial gravities within the chamber.

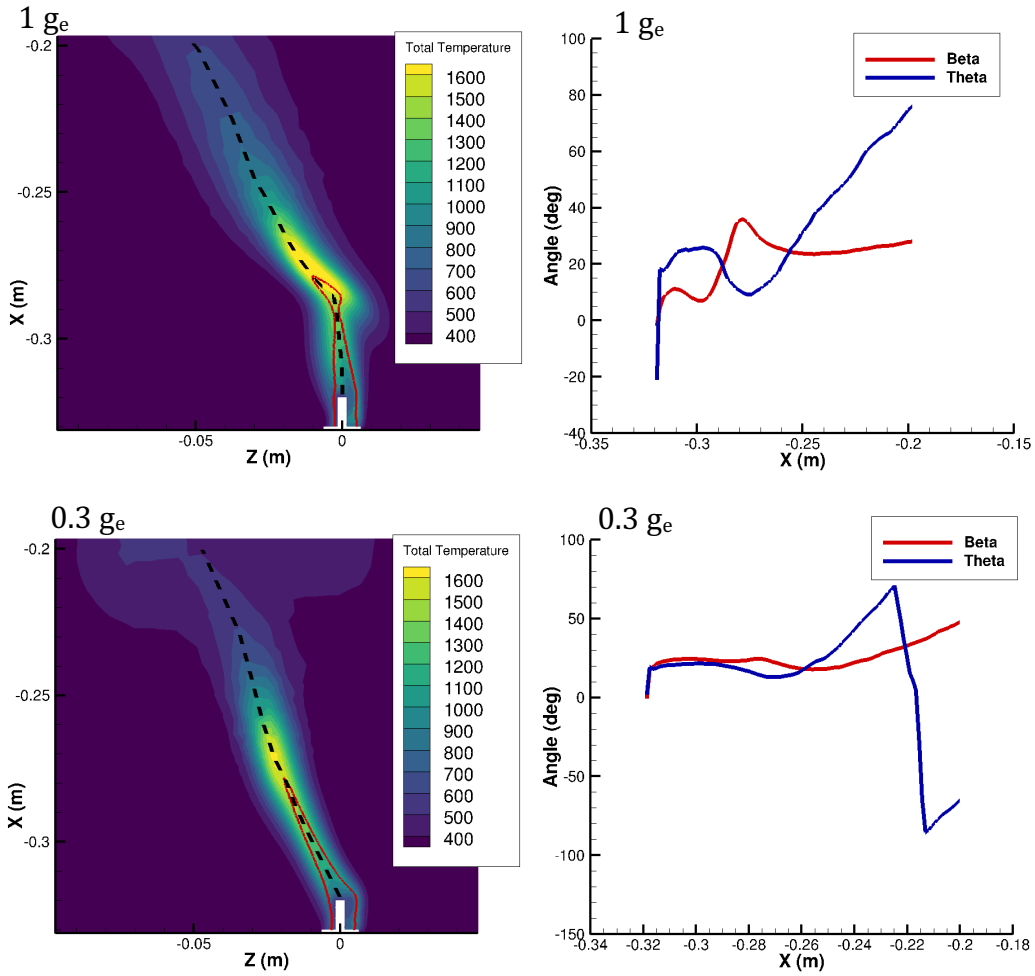

Figure 4-14. θ and β vs. X coordinate for 1, and 0.3 g_e

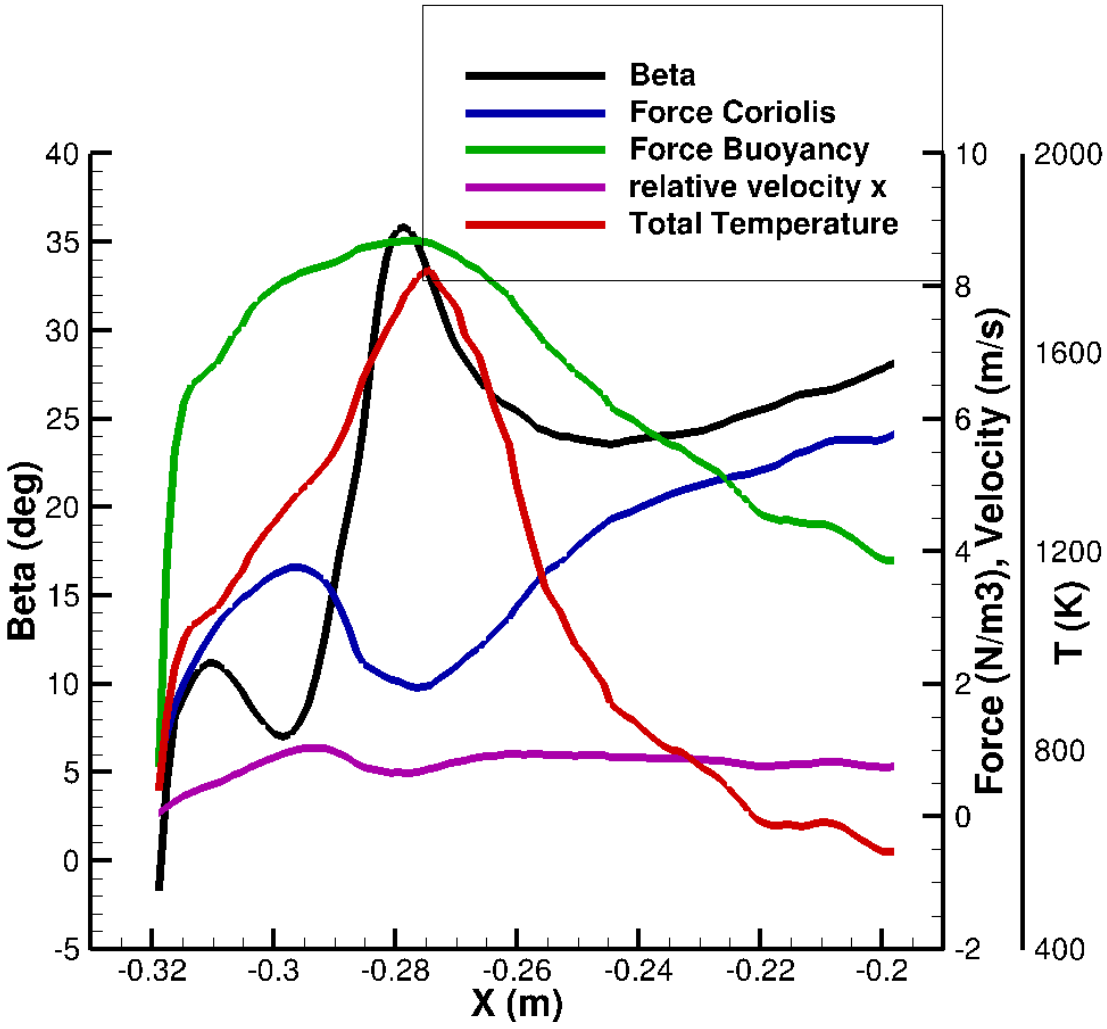

Figure 4-15. β, Coriolis Force, Buoyancy Force, Relative Velocity in *x* direction, and Total temperature for $1g_e$ flame

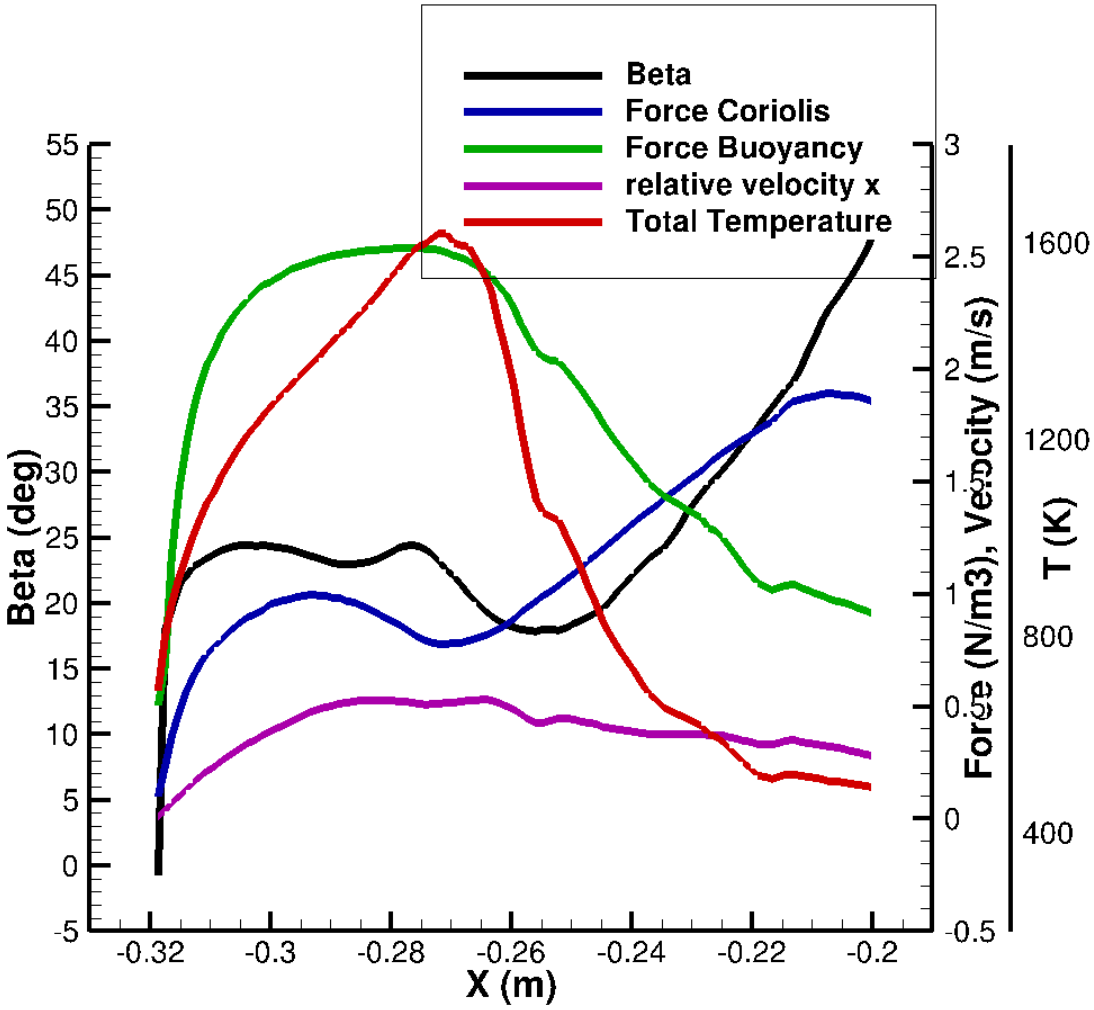

Figure 4-16. β, Coriolis Force, Buoyancy Force, Relative Velocity in *x* direction, and Total temperature for $0.3g_e$ flame

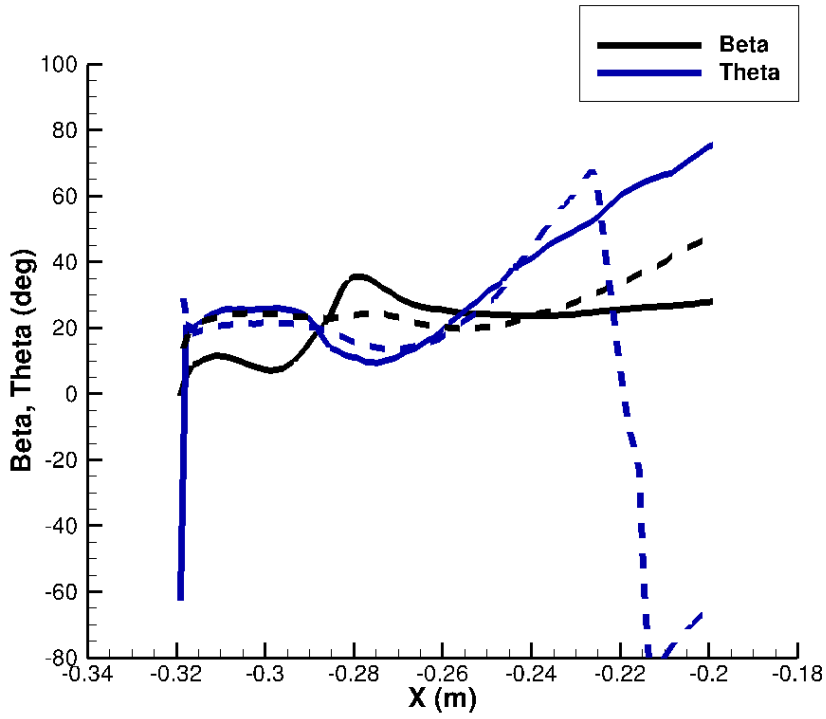

Figure 4-17. β, and θ for 1 and 0.3g_e flame. (0.3g_e is dashed)

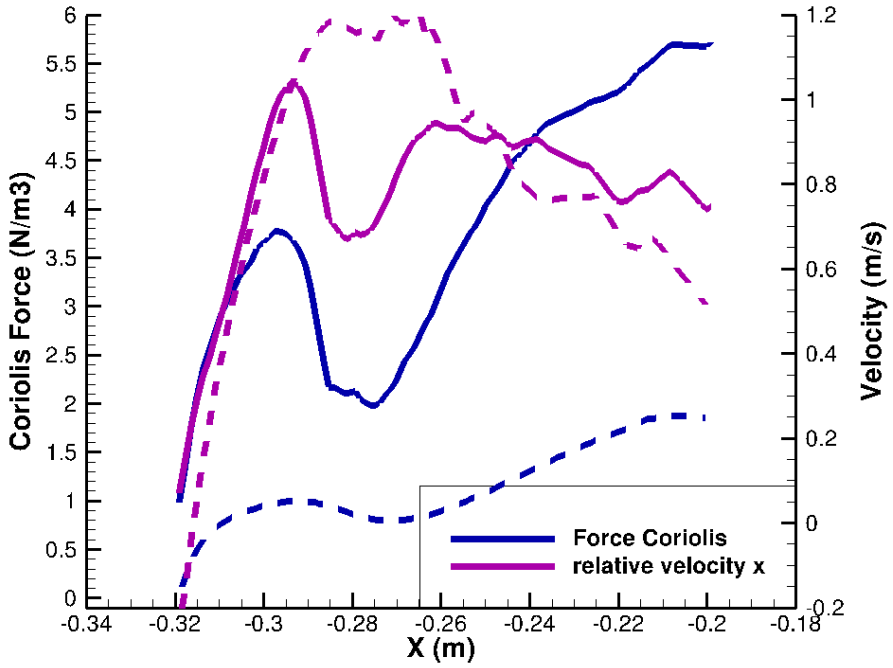

Figure 4-18. Coriolis Force and Velocity for 1 and 0.3g_e flame. (0.3g_e is dashed)

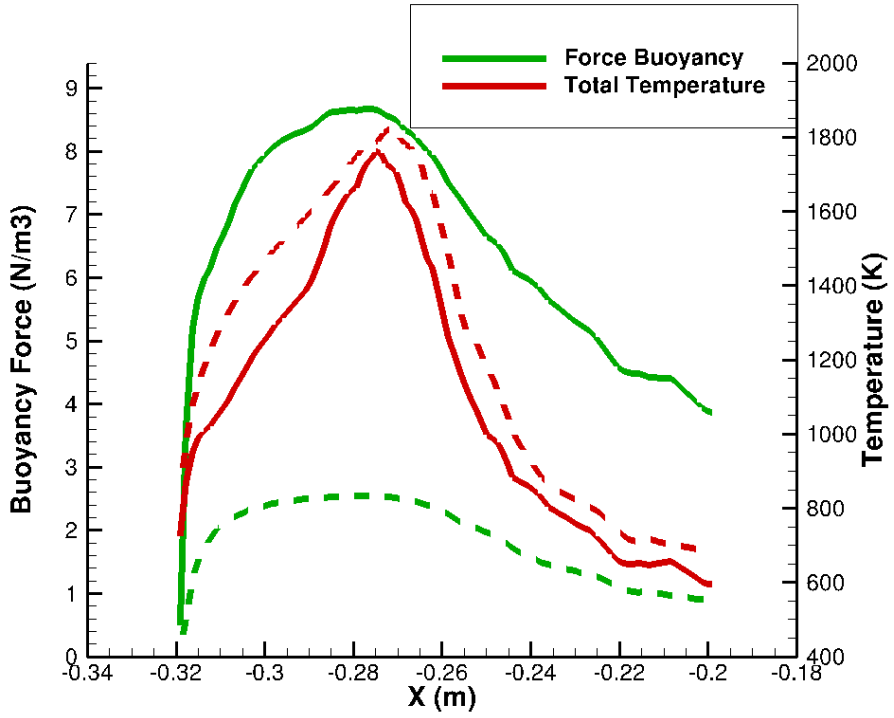

Figure 4-19. Buoyancy Force, and Temperature for 1 and $0.3g_e$ flame. ($0.3g_e$ is dashed)

4.3 Recirculation

From Figure 3-1 and Figure 3-2 it is clear that the simulation is producing data that was close to experiments but there is one factor that was not matching the expected results. Upon looking at the $1g_e$ and $0.59g_e$ flames from Figure 3-2 it is noticed that the bottom part of the flame seems to be going vertically unlike the experimental images which have a clear tilt in that section.

To see how the flame was behaving and with the intent of finding the source of that anomaly, a simulation was performed with 700 time steps and an end time set to 7s instead of 5s. Figure 4-20 shows the result of the simulation at t = 7s. In this figure, the flame has already shifted from its vertical and left leaning position to the right tilted position. The white streamlines show the direction of the air velocity

inside the chamber and can be seen pushing the flame towards right direction i.e., in opposite to the Coriolis force.

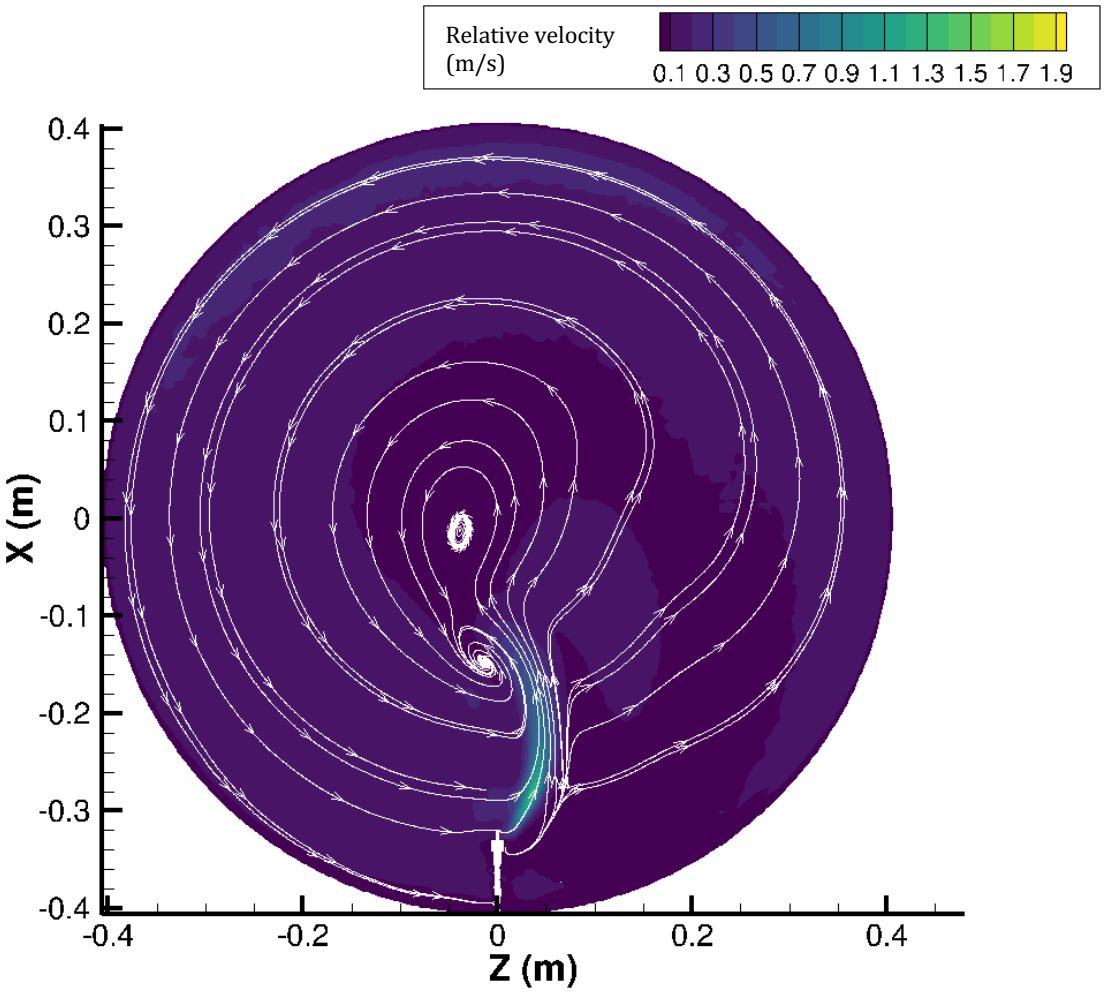

Figure 4-20. Numerical simulation flame at 7 s. The white lines are the streamlines of relative velocity (m/s). Artificial gravity level: 1 g_e.

In order to see how this develops, Figure 4-21 shows the flame growth of a 1 g_e flame throughout 7 s. One can see that the flame first tilts left as expected but as time passes it leans more and more to the opposite side. Thus, no longer matching anymore the experimental results where the flame always remained tilted in one direction (Figure 3-1). From Figure 4-21, it appears that this phenomenon occurs due to the establishment of recirculation within the chamber..

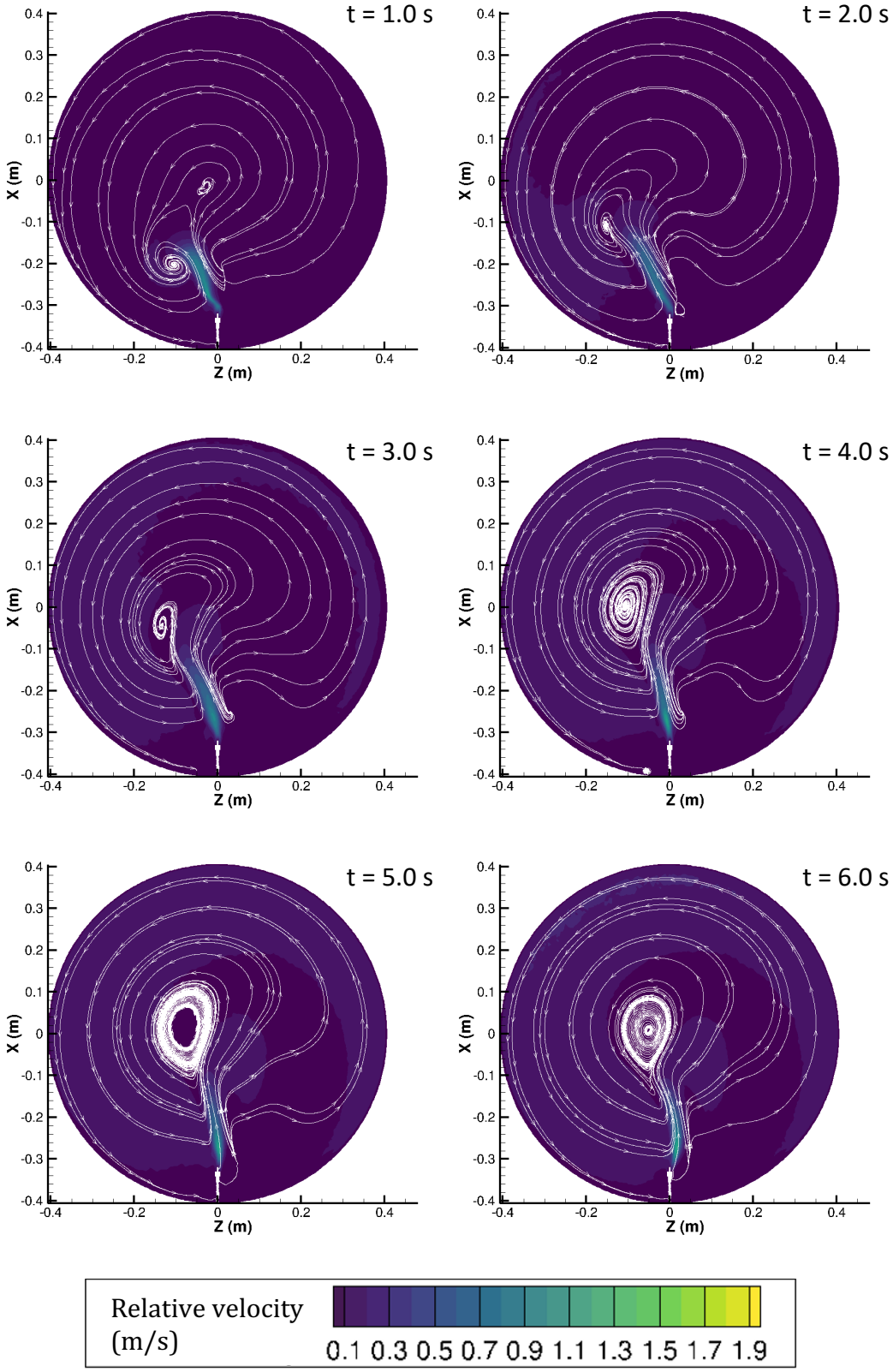

Figure 4-21. Flame growth of numerical simulation in the first 6 s at an equal interval of 1 s. The white lines are the streamlines of velocity. Artificial gravity level: 1 g_e.

Since the chamber is closed, hot combustion gases start circulating inside the chamber, eventually moving back to the combustion zone. However, recirculation of these gases takes place in the opposite direction of centrifuge rotation and the Coriolis acceleration (Figure 4-20 and Figure 4-21). Figure 4-22 depicts the dynamics of flow recirculation. This recirculation is caused by the air movement due to the buoyancy force on the hot reactants from the combustion. In Figure 4-22a, it can be noticed that for an open geometry, the flame shape always remains vertical due to hot buoyant gases rising upwards, and it is not tilted due to the absence of recirculation. On the other hand, when the flow remains inside a closed geometry (Figure 4-22b), it creates a recirculation that affects the shape of the flame tilting it in one direction. Note that the recirculation in the chamber is not symmetric and the diagram shown in Figure 4-22b is only notional. In the simulation, the recirculation was noticed to dominate on one side and that is due to the flame not being symmetric. Had the flame not experienced Coriolis force, we could expect the recirculation to be symmetric. This explanation also aligns with the results at lower gravities in which the recirculation can't be perceived. The recirculation is ultimately based on the rotation speed of the chamber. The higher the centripetal acceleration, the faster the chamber is rotating and thus recirculation flows develop faster. In this case, for the lower gravities, the buoyancy force is indeed lower and recirculation ends up being lower than in higher gravity cases. However, when the recirculating flow is strong enough, it may push the flame back to the vertical direction (observed in the $1g_e$ simulated case but not in the experiment due to short duration and reasons discussed in the below section). In lower gravity cases (<0.075

g_e), the Coriolis effect is also less pronounced, and the flame is closer to being symmetric (vertical). If the flow recirculation were to occur, it would be expected to be more symmetric (as in Figure 4-22b).

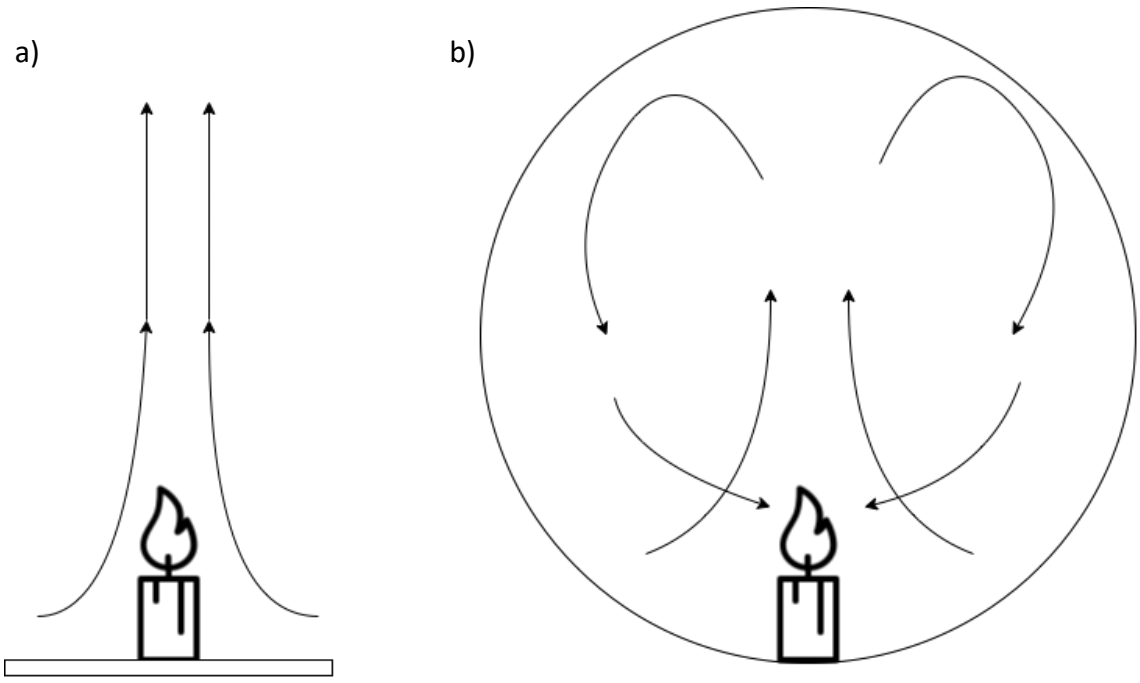

Figure 4-22. The expected flow of air around a flame in an open container (a) vs. in a closed container (b)

It is thought that fully-formed recirculation is less prevalent in the experimental results due to the chamber being full of equipment's like cameras, sensors, cables, mounts, as well as other materials necessary for the realization of centrifuge experiments that obstruct the flow of the air. The simulation results presented so far assumed the chamber was empty with only a liquid wick inside. To make the chamber geometry closer to reality, random interior objects are distributed inside the chamber.

The new chamber geometry is similar to that shown in Chapter 2 with the addition of cylindrical shaped structures of different sizes to mimic the equipment such as cables, cameras, and fixtures in the actual experimental setup. The "anti-recirculation" geometry was made following the same mesh specifications as the previous model and setup in ANSYS Fluent using the same initial and boundary conditions. Figure 4-23 shows the new anti-recirculation geometry.

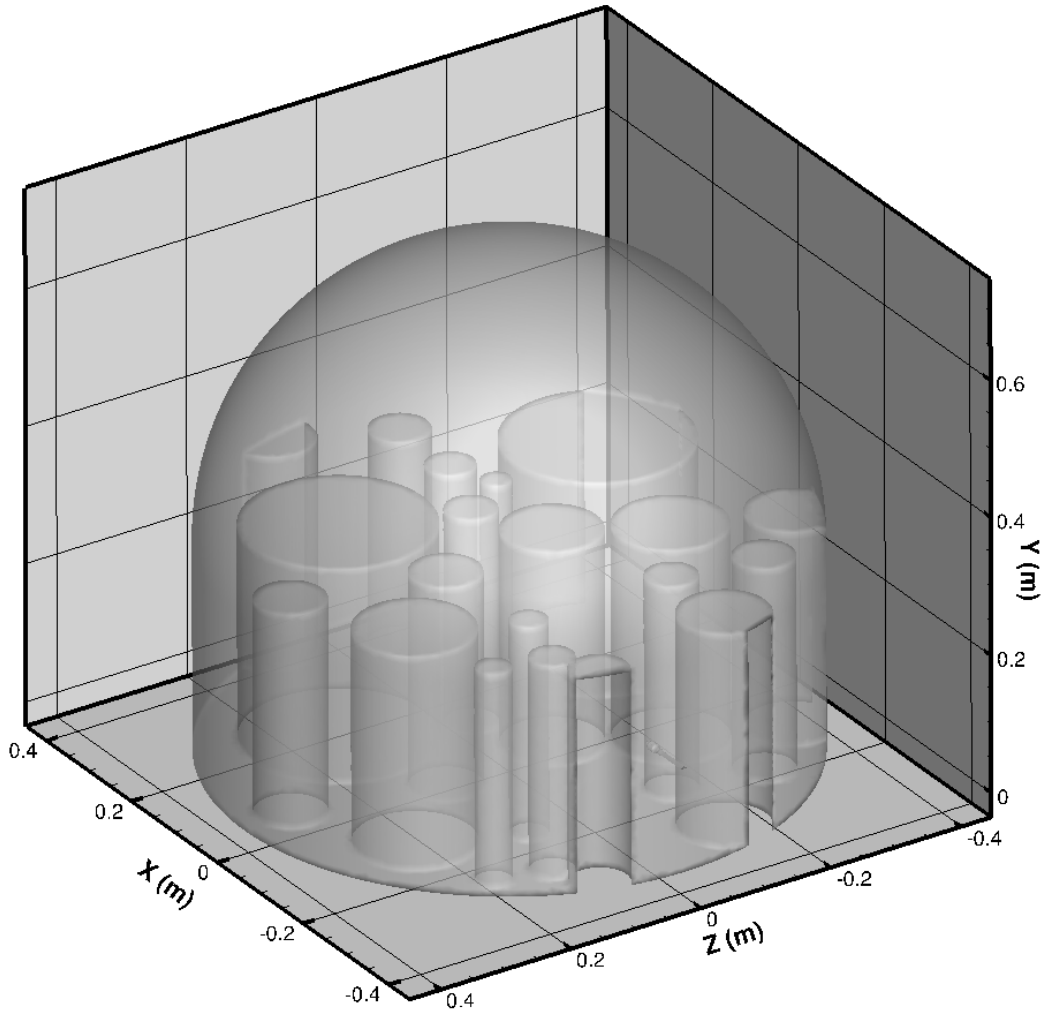

Figure 4-23. 3D numerical domain of anti-recirculation geometry

Figure 4-24 shows the geometry and flame for a simulated gravity of $1g_e$ when time is 10s (well ahead of the experiment time). It is noticeable that unlike the flames in

Figure 4-21, this flame is not tilting so it is considered that the recirculation has been removed. The same is seen in Figure 4-25 which is that of a flame in simulated 0.3 g_e also when time is 10s. These figures demonstrate that the "anti-recirculation" geometry is appropriate to remove the recirculation within the chamber. The simulation results in previous sections 4.1, and 4.2 are still correct as the recirculation doesn't take place until time is larger. In addition, recirculation takes place over even a longer amount of time when the chamber rotation is slower.

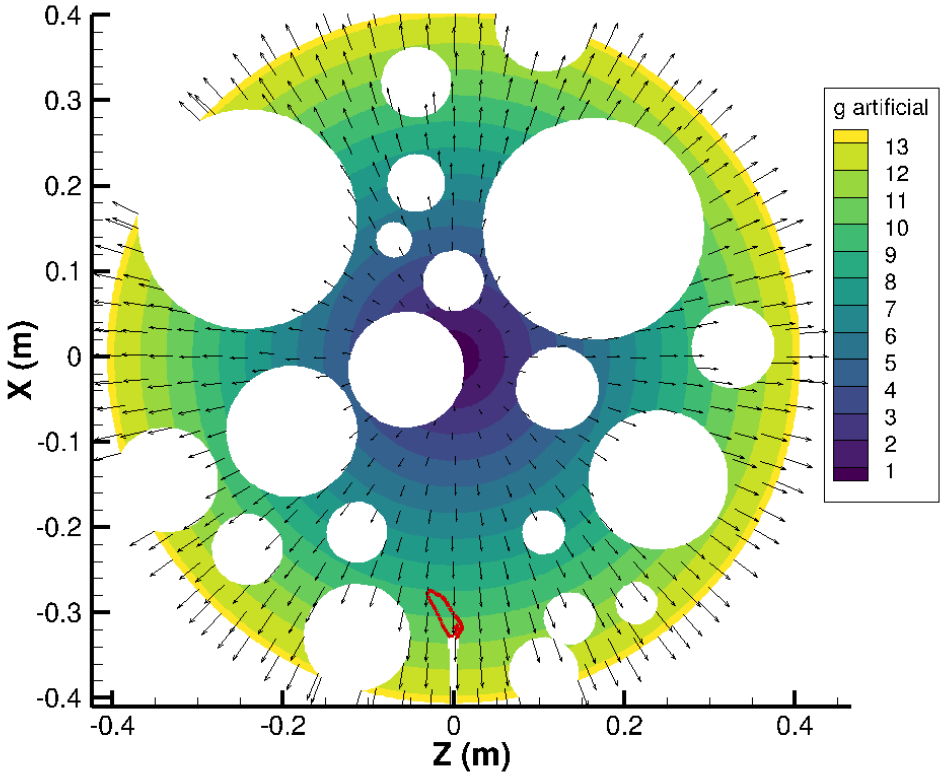

Figure 4-24. Simulated 1g_e flame at t = 10s. Contours of perceived local artificial gravity

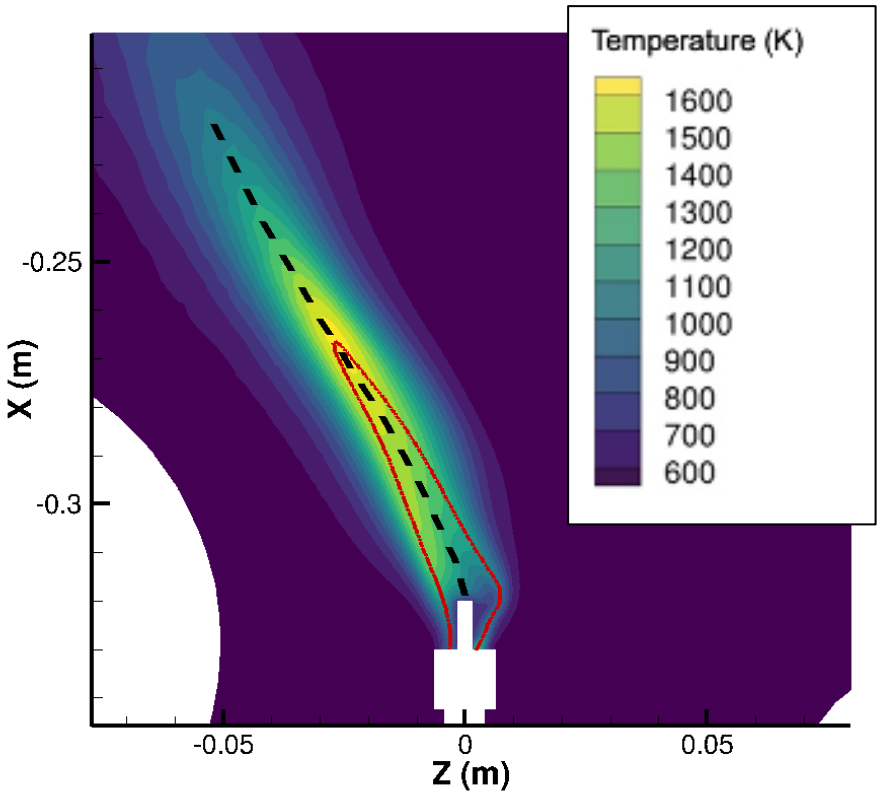

Figure 4-25. Simulated 0.3 g_e flame at t = 10s. Contours of Temperature

5 Conclusions and Future Work

5.1 Conclusions

A numerical model is developed to investigate the flame dynamics in a partial gravity environment created by a rotating centrifuge. Heptane fuel is burned in a candle wick configuration at 32 cm from the axis of rotation. Different artificial partial gravity levels (0, 0.003 g_e, 0.012 g_e, 0.075 g_e, 0.2 g_e, 0.3 g_e, 0.59 g_e, and 1 g_e) are obtained by varying the rotational speed of the centrifuge. Simulations are compared with experiments and the effect of Coriolis force and recirculation is presented. Key findings are as follows.

1) The model successfully simulated the flames at different artificial g levels, with good agreements in flame shape and flame tilt angles with the experiment results.
2) Flow recirculation in the limited volume of the combustion chamber affects the fire behavior. For the artificial $1g_e$ simulated case, the flame is tilted to the left for the first 3-4 seconds, after which the recirculating flow overcomes the Coriolis acceleration and pushes the flame back to its neutral position (i.e., being straight). However, this was not observed in the experiments.
   For other artificial gravity levels (i.e., < $1g_e$), buoyancy flow and flow recirculation are weaker and so the flame remains tilted to the left for the whole simulated 5s duration.

3) It is suggested that future centrifuge experiments in which buoyancy flows are high, take into consideration recirculation effects and add measures to counter it within the chamber.
4) The Coriolis force is responsible for tilting the flame mostly in the tangential direction (i.e., to the left of the flame). The maximum Coriolis acceleration is found to increase linearly with the artificial gravity level.
5) For higher g_e cases, when the velocity in the radial direction is strong enough, the Coriolis force grows and bends the flame into a sharper angle. This however is short lived as when the flame bends, the Coriolis force decreases in the tangential direction.

5.2 Future Work

The current project has several avenues of future work that can be performed. The focus of the simulation is to mimic the rotation chamber and study the Coriolis force. With a good simulation, we will be able to simulate other experiments done in that same chamber that is used to conduct partial gravity experiments. In addition, knowing how the Coriolis effect acts is the first step in finding a method of countering the Coriolis effect on the flame by the use of an air jet stream or confinement. In order to accomplish these steps, the simulation has to simulate experiments more accurately and for that, the following future work will help achieve that goal:

1) Simulation of the case at true $1g_e$. In order to obtain more data on how the Coriolis force acts on the flame, conducting a simulation of the case in $1g_e$

would allow us to compare it with the experimental images of true $1g_e$ and rotational $1g_e$.

2) Using a User Defined Function (UDF) instead of a constant mass flow rate for the fuel inlet. While the current approach is a good estimate, by using a correctly implemented UDF to correlate the flame heat feedback and the fuel mass flux on the wick surface, the simulated candle should give results even closer to experiments than the current ones.

In addition, the Reynolds number (shown in the Appendix) for the flow was found to be in the laminar region (<2000). Thus, it is recommended that for future simulations the flow be considered laminar in nature within the chamber. This will result in much lower computational times.

Appendix

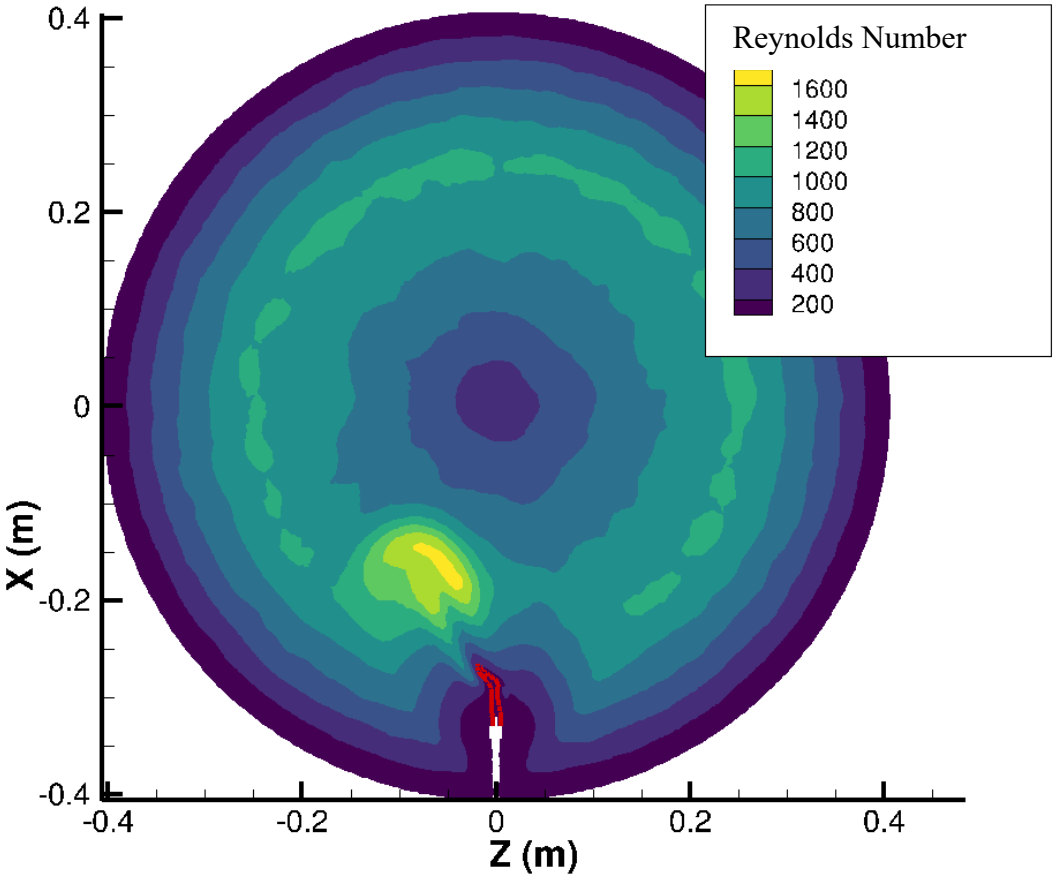

Appendix Figure 0-1. Reynolds number for domain in 1 g_e flame simulation

Bibliography

[1] K. R. Sacksteder and J. S. Tien, "Buoyant downward diffusion flame spread and extinction in partial-gravity accelerations," *Symposium (International) on Combustion*, vol. 25, no. 1, pp. 1685–1692, 1994, doi: 10.1016/S0082-0784(06)80816-7.

[2] X. Zhao, Y.-T. T. Liao, M. C. Johnston, J. S. T'ien, P. v. Ferkul, and S. L. Olson, "Concurrent flame growth, spread, and quenching over composite fabric samples in low speed purely forced flow in microgravity," *Proceedings of the Combustion Institute*, vol. 36, no. 2, pp. 2971–2978, 2017, doi: 10.1016/j.proci.2016.06.028.

[3] D. L. Urban *et al.*, "Flame spread: Effects of microgravity and scale," *Combust Flame*, vol. 199, pp. 168–182, Jan. 2019, doi: 10.1016/j.combustflame.2018.10.012.

[4] S. L. Olson, P. v. Ferkul, and J. S. T'ien, "Near-limit flame spread over a thin solid fuel in microgravity," *Symposium (International) on Combustion*, vol. 22, no. 1, pp. 1213–1222, Jan. 1989, doi: 10.1016/S0082-0784(89)80132-8.

[5] A. Carney, Y. Li, Y.-T. Liao, S. Olson, and P. Ferkul, "Concurrent-flow flame spread over thin discrete fuels in microgravity," *Combust Flame*, vol. 226, pp. 211–221, Apr. 2021, doi: 10.1016/j.combustflame.2020.12.005.

[6] I. I. Feier, H.-Y. Shih, K. R. Sacksteder, and J. S. Tien, "Upward flame spread over thin solids in partial gravity," *Proceedings of the Combustion*

Institute, vol. 29, no. 2, pp. 2569–2577, Jan. 2002, doi: 10.1016/S1540-7489(02)80313-3.

[7] J. Kleinhenz, I. I. Feier, S.-Y. Hsu, J. S. T'ien, P. v. Ferkul, and K. R. Sacksteder, "Pressure modeling of upward flame spread and burning rates over solids in partial gravity," *Combust Flame*, vol. 154, no. 4, pp. 637–643, Sep. 2008, doi: 10.1016/j.combustflame.2008.05.023.

[8] K. R. Sacksteder, P. S. Greenberg, R. D. Pettegrew, J. S. Tien, P. v. Ferkul, and H.-Y. Shih, "Forced Flow Flame Spreading Test: Preliminary Findings from the USMP-3 Shuttle Mission," in *Forced Flow Flame Spreading Test: Preliminary Findings From the USMP-3 Shuttle Mission*, Nov. 1998.

[9] Y. Li, Y.-T. T. Liao, P. v. Ferkul, M. C. Johnston, and C. Bunnell, "Experimental study of concurrent-flow flame spread over thin solids in confined space in microgravity," *Combust Flame*, vol. 227, pp. 39–51, May 2021, doi: 10.1016/j.combustflame.2020.12.042.

[10] J. Park, J. Brucker, R. Seballos, B. Kwon, and Y.-T. T. Liao, "Concurrent flame spread over discrete thin fuels," *Combust Flame*, vol. 191, pp. 116–125, May 2018, doi: 10.1016/j.combustflame.2018.01.008.

[11] S. M. Dakka, "Theoretical prediction of critical pyrolysate mass fluxes of a material to mitigate spacecraft or planetary habitat fire," *Journal of British Interplanetary Society*, vol. 70, pp. 12–18, Aug. 2017.

[12] S. L. Olson and P. Ferkul, "Evaluating Material Flammability in Microgravity and Martian Gravity Compared to the NASA Standard

Normal Gravity Test," in *42nd International Conference on Environmental Systems*, Jul. 2012. doi: 10.2514/6.2012-3492.

[13] A. Hamins, J. C. Yang, and T. Kashiwagi, "An experimental investigation of the pulsation frequency of flames," *Symposium (International) on Combustion*, vol. 24, no. 1, pp. 1695–1702, Jan. 1992, doi: 10.1016/S0082-0784(06)80198-0.

[14] C.-B. Jiang, J. S. Tien, and H.-Y. Shih, "Model calculation of steady upward flame spread over a thin solid in reduced gravity," *Symposium (International) on Combustion*, vol. 26, no. 1, pp. 1353–1360, Jan. 1996, doi: 10.1016/S0082-0784(96)80354-7.

[15] S.-Y. Hsu and J. S. T'ien, "Flame spread over solids in buoyant and forced concurrent flows: Model computations and comparison with experiments," *Proceedings of the Combustion Institute*, vol. 33, no. 2, pp. 2433–2440, Jan. 2011, doi: 10.1016/j.proci.2010.05.093.

[16] P. Ferkul, "Zero-Gravity Centrifuge: A Rotating Facility for Obtaining Arbitrary Centrifugal Accelerations in Drop Tower Experiments," *National Center for Space Exploration Research*. 2008.

[17] A. Zatania Lojo, A. Sharma, Y.-T. Liao, M. Johnston, and P. Ferkul, "A Numerical Study of Liquid Fuel Wick Flames in Artificial Partial Gravity in a Centrifuge Facility," in *International Conference on Environmental Systems*, Jul. 2022.

[18] ANSYS. Inc, "ANSYS Fluent 12.0 Theory Guide," Jan. 23, 2009.

[19] A. Hamins, M. Bundy, and S. Dillon, “Characterization of Candle Flames,” *Journal of Fire Protection Engineering*, vol. 15, no. 4, pp. 265–285, Nov. 2005, doi: 10.1177/1042391505053163.

[20] PubChem, “PubChem Compound Summary for CID 8900, Heptane,” *National Center for Biotechnology Information*, Nov. 15, 2022.